Catalytic partial oxidation of methane to synthesis gas: Materials and reaction mechanisms.

Federica Mudu

Department of Chemistry

University of Oslo

A thesis submitted for the degree of

PhilosophiæDoctor (PhD)

2011

Series of dissertations submitted to the
Faculty of Mathematics and Natural Sciences, University of Oslo
No. 1127

ISSN 1501-7710

Cover: Inger Sandved Anfinsen.
Printed in Norway: AIT Oslo AS.

Produced in co-operation with Unipub.
The thesis is produced by Unipub merely in connection with the
thesis defence. Kindly direct all inquiries regarding the thesis to the copyright
holder or the unit which grants the doctorate.

Acknowledgements

When I started this PhD adventure I knew nothing about catalysis, and even less about structural inorganic chemistry. The only thing I knew was that I still wanted to learn more chemistry, and it became possible thanks to the work of 3 great supervisors.

I will always be deeply grateful to you Unni, for showing me with enthusiasm how much fun and struggle catalysis can be, for never giving up on me or on this challenging project and for taking care of me when I most needed.

Thank you Helmer, for opening up the endless world of refinements and much, much more structural inorganic chemistry for me; now that I don't have to run GSAS anymore I can tell it has been great fun!

Bjørnar, thank you for all the hours you spent discussing those thousand methane pulses results with me, you will surely find traces of those discussions in all the articles we wrote!

PhD life is much more than reactors and articles writing, it has been fantastic to share frustrations, achievements, dinners, lunches, parties, breakfasts and countless cups of tea and cappuccino with each of you; Laurent, Francesca, Karina, Kai, Cristoph, Aga, Mari, Hiroshi, Pascal, Yael, Rune, Rene.

Mamma e pap, senza il vostro supporto morale e economico la mia avventura norvegese non sarebbe mai diventata realt, e con lei neanche questo dottorato; grazie di cuore.

E infine, Are, mio compagno di vita e alleato in ogni battaglia e conquista; grazie di essere sempre al mio fianco a sostenermi in ogni scelta e nel mio cuore a riscaladare i lunghi inverni norvegesi.

Contents

List of Figures

LIST OF FIGURES

Glossary

CPO	Catalytic partial oxydation
F-T	Fischer-Tropsch
SMR	Steam methane reforming
ATR	Autothermal reforming
POX	Partial oxidation
LSF	$La_{1-x}Sr_xFeO_{3-\delta}$
LSC	$La_{1-x}Sr_xCoO_{3-\delta}$
PDF	Powder Diffraction File
PUS	Powder Universal Spectrometer
SSITKA	Steady state isotopic transient kinetic analysis setup
STP	Standard temperature and pressure
MS	Mass Spectrometer
MFC	Mass flow controller
XRD	X-ray diffraction
NPD	Neutron powder diffraction
TGA	Thermogravimetric analysis
XPS	X-ray photoelectron spectroscopy

LIST OF FIGURES

1

Introduction

1.1 Background and Motivation

Depleting oil reserves, combined with novel technology for exploiting remote natural gas, makes natural gas an increasingly attractive raw material for the chemical industry[1].

Fischer-Tropsch gas to liquids technology (F-T) and methanol synthesis (equations 1.5 and 1.6 respectively) are two ways of converting natural gas to more valuable and easily transportable chemicals (liquids)[2]. The fact that methane is the main component of North Sea natural gas (> 94 %)[3] makes these processes relevant in a Norwegian perspective.

The first step in these processes is the conversion of natural gas to synthesis gas (a mixture of carbon monoxide and hydrogen) followed by the synthesis of methanol from synthesis gas. Today, synthesis gas production from natural gas is usually carried out by steam reforming (equation 1.1) and/or auto thermal reforming (equation 1.4, 1.1 and 1.2) technologies[3].

In methane steam reforming, methane is reacted with water vapor at temperatures as high as 1273 K to produce syngas with a ratio of CO:H_2 of 1:3. The high temperature required for the reforming reaction makes this process highly energy intensive, moreover the ratio between CO and H_2 is not suitable for direct methanol or higher hydrocarbons (F-T) synthesis and requires a secondary water gas shift unit to optimize it.

In the autothermal reforming process methane reacts first with oxygen (equation 1.4, the energy released in this exothermic combustion step is used for the endothermal

reforming reaction between the unreacted methane and the combustion products, water and carbon dioxide (equation 1.1 and 1.2).

$$CH_4 + H_2O \Leftrightarrow CO + 3H_2 \tag{1.1}$$

$$CH_4 + CO_2 \Leftrightarrow 2CO + 2H_2 \tag{1.2}$$

$$CH_4 + 2O_2 \rightarrow CO_2 + 2H_2O \tag{1.3}$$

$$CH_4 + 1/2O_2 \rightarrow 1/4CO_2 + 1/2H_2O + 3/4CH_4 \tag{1.4}$$

$$(2n+1)H_2 + nCO \rightarrow C_nH_{2n+2} + nH_2O \tag{1.5}$$

$$CO + 2H_2 \rightarrow CH_3OH \tag{1.6}$$

Recently an alternative approach to methane conversion to syngas has received increasing attention[4]. This approach belongs to the class of so called forced periodic processes[5,6]. The reaction is here divided in two steps that proceed separately in space and time, the solid catalyst acts now also as reactant and the gas phase reaction is splitted to two gas-solid reactions.

In the specific case which forms the basis of this thesis, in a first step, methane reacts with a metal oxide, the metal oxide is being reduced and methane is being converted to oxygenated products (CO_2, CO, H_2O) and H_2. In a second step the metal oxide is then reoxidized with air. A schematic illustration of this process is shown in Figure 1.1.

The reaction can be run continuously, if two reactors are used and the solid is circulated between them, or discontinuously, if only one reactor is used and the gas feed is periodically switched between reductant (methane) and oxidant (air).

There are several advantages in separating the overall (Catalytic partial oxydation) reaction in two steps, the most relevant ones are[4,7]:

- No explosive gas mixture are formed, hydrocarbons can be fed at high concentration (no direct mixing between oxygen and hydrocarbons takes place)

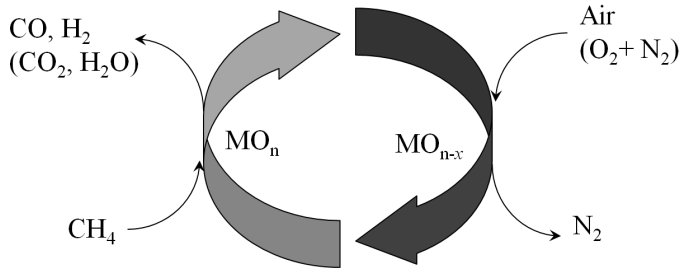

Figure 1.1: Reaction Concept - Schematic representation of the cyclic oxidation of methane with a metal oxide

- Air can be used as oxidant without resulting in product dilution
- The two reaction steps can be optimized separately
- Non selective reactions due to gas phase oxygen may be avoided, higher yields in the desired products may be achieved

These advantages are accompanied by a number of drawbacks. The high amount of metal oxide needed to run the reaction at industrial level is probably dominating among them. Furthermore, the selected oxide must accomplish a number of chemical and structural requirements, mainly related to the reduction-oxidation stability. Moreover, additional specific equipment is required depending on the process design.

In spite of these drawbacks this reaction concept has been studied for several oxidation and dehydrogenation reactions. Among them, oxidative coupling of methane[8], oxidative dehydrogenation of butane and propane[9–14], butane oxidation to maleic anhydride[15,16], oxidation of propene to acrolein[17], oxidation of acrolein to acrylic acid[18] and dehydrogenation of alkanes[19,20].

1.1.1 The remote gas challenge

A considerable amount of the natural gas reserves discovered but not yet exploited are located in remote locations. With increasing demand in fossil fuels, exploiting these reserves might become economically viable and this calls for proper technological solutions. Natural gas fields in remote locations are often small, this makes pipelines not a suitable solution for the transfer of the gas onshore. Methanol is a liquid product

and is therefore easier to transport onshore via vessels. Converting natural gas to methanol offshore, on a floating unit, is one of the candidate processes for utilization of these reserves.

The principal technologies for producing syngas from natural gas are: catalytic steam methane reforming (SMR), two-step reforming, autothermal reforming (ATR), partial oxidation (POX), and heat exchange reforming.

Adapting these technologies for offshore applications in small floating units has proved to be a challenging issue. Methane steam reforming produces syngas with a CO/H_2 lower than what needed for the downstream methanol production and requires therefore additional steps for adjusting this ratio. Autothermal reforming on the other hand delivers syngas with a correct CO/H_2 ratio but requires oxygen as reactant. Oxygen production and storage off shore in a floating unit is to be avoided for obvious safety and economical reasons.

The conversion of methane to syngas through CPO reaction with a metal oxide can deliver a correct CO/H_2 ratio for methanol production and does not require oxygen (can be run with air without product dilution), it might therefore be developed into a technology for offshore plants.

The reducible oxide used as oxygen carrier must satisfy a number of requirements[21]:

- A high oxygen exchange capacity
- Fast oxygen exchange kinetics at the reaction temperature
- Should withstand the harsh environment of the partial oxidation reaction
- Catalytically active, or possible to combine with an active catalyst, for methane decomposition
- Relatively easy to synthesize and cost effective

Based on the listed requirements, ceramic non stoichiometric oxides represent a suitable class of materials for this purpose. Indeed, most of the published works, dealing with methane conversion to syngas with lattice oxygen (as describe in more detail in the following sections), involve the use of non stoichiometric oxides.

Mainly two classes of non stoichiometric oxides have been attracting attention as active materials for cyclic conversion of methane to syngas, perovskites with the general

formula $A_{1-x}A'_xBO_3$ where A is a rare earth ion, A' is usually Sr and M is Co, Mn, Cr, Fe or mixtures of these; and CeO_2 based ceramic materials eventually mixed with ZrO_2, Sm_2O_3 or similar rare earth metal oxides. A brief overview of the literature results obtained with these two classes of materials is given in sections 1.1.2 and 1.1.3.

The aim of this PhD work has been to study the reaction of methane with two different classes of reducible oxides (ceria based, and perovskite based) at temperatures around 873 K. Focus has been given to the factors governing reaction selectivity and the relationship between oxides structure and reaction products.

1.1.2 Ceria based oxygen carriers

Cerium dioxide (CeO_2) crystallizes in the fluorite structure, a face-centered cubic unit cell where each cerium cation is coordinated to 8 oxygen atoms at the corners of a cube as illustrated in Figure 1.2.

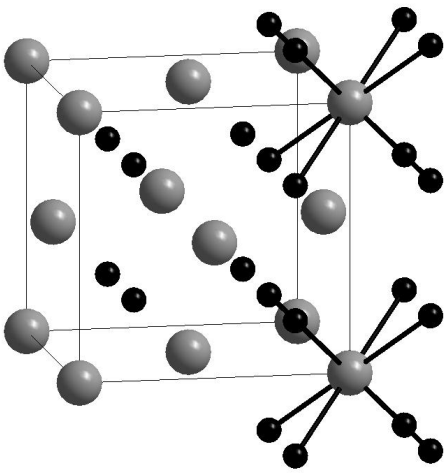

Figure 1.2: Ceria Structure - The crystal structure of CeO_2, oxygen atoms in black and cerium atoms in dark grey

Depending on temperature and partial pressure of oxygen, cerium oxides in the composition range Ce_2O_3-CeO_2 can be formed[22].

The consequences of doping CeO_2 with zirconium has been extensively studied since the 1950s[23] due to the importance of these materials in the fields of solid oxide fuel cells and ceramics. CeO_2 and ZrO_2 form solid solutions for a wide range of compositions and the phase diagram has been extensively studied[24–28]. A monoclinic ($P2_1/c$), a cubic (Fm3m) and three tetragonal phases termed t, t‘ and t“ (all space group $P4_2/nmc$) are reported for temperatures below 1273 K[29–31]. Their existence regions are indicated in the upper abscissa in Figure 1.3. The three tetragonal phases are characterized by the degree of tetragonal distortion (c/a) and by their nature (t is stable, while t‘ and t“ are metastable). The distinction between these phases, especially between the t and t‘, and between t“ and cubic is quite subtle and can hardly be settled by laboratory scale powder X-ray diffraction. The ionic radius of Zr is smaller than the one of Ce , as a consequence, the unit cell size of the solid solutions decreases proportionally to the Zr content as reported in Figure 1.3[32].

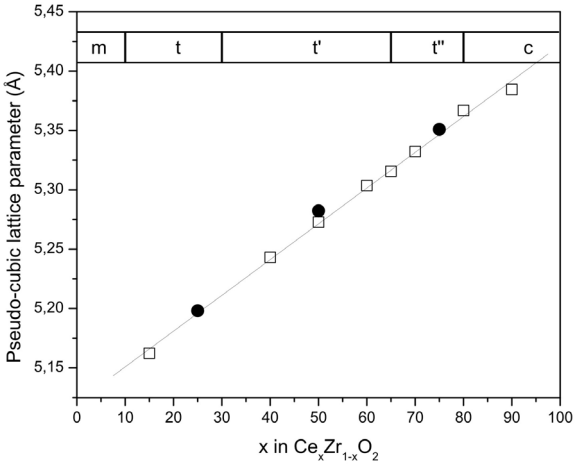

Figure 1.3: Ceria Zirconia solid solution unit cell size - The pseudocubic unit cell size in ceria-zirconia solid solutions as a function of Ceria content, the solid data points are values obtained in this work (paper 2) while the empty data points are reported from literature[33].

The behavior and the activity of ceria based oxides in catalysis is typically related

with the redox couple Ce^{4+}/Ce^{3+} and the consequent reversible oxygen storage capacity. Ceria based oxides have a great potential for catalytic applications, and have during the last years been investigated for processes like water gas shift, supports for reforming catalysts, VOCs catalytic combustion, CO preferential oxidation and conversion of emission gases[34–43].

The introduction of Zr into the CeO_2 framework has important consequences on the redox behavior of the resulting solid solutions as illustrated in Figure 1.4.

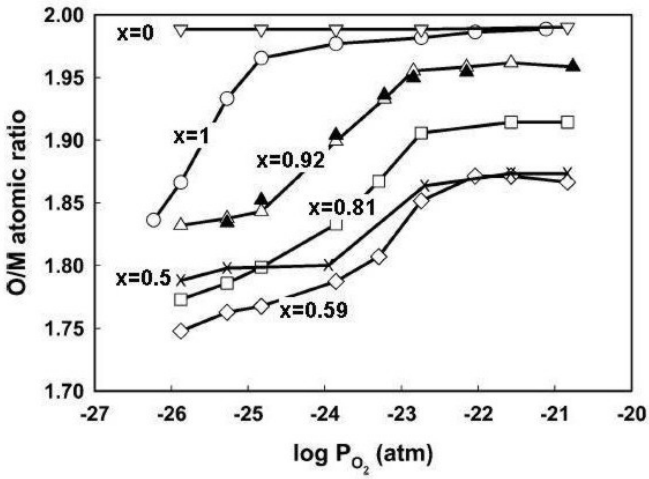

Figure 1.4: Nonstoichiometry of ceria-zirconia solid solutions - Oxygen to metal ratio (O/(Zr + Ce)) as a function of oxygen partial pressure for $Ce_xZr_{1-x}O_{2-\delta}$[44].

The correlation between the redox properties and the reaction behavior between the various oxides and methane has been investigated in detail in this PhD study.

1.1.3 Perovskite based oxygen carriers

Perovskite type oxides are a class of oxides characterized by the general formula ABO_3. The ideal structure is cubic with the B cation in 6-fold coordination surrounded by an octahedron of oxygen atoms and the A cation located in the large interstices, surrounded by eight octahedra, leading to a AO_{12} polyhedron. In order for the oxide to crystallize in the ideal cubic structure the size relationship between ionic radii for A and B cation

must be so that $(R_A + R_O)/\sqrt{2}(R_B + R_O) = t = 1$[45].

In most cases however a size mismatch between A and B cations leads to t values above or below 1, in these cases perovskite phases of non ideal symmetry (non cubic) can be formed. The most common variants of perovskite type are represented by orthorhombic and rhombohedral distortions of the ideal cubic unit cell. A representation of the cubic and distorted orthorombic structures is shown in Figure 1.5.

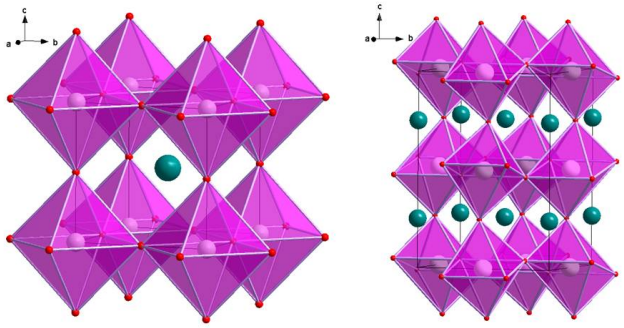

Figure 1.5: Perovskite structure - Structure of perovskite oxide with chemical formula ABO_3. The red spheres are O atoms, the white spheres are B atoms, and the teal spheres are the A atoms. On the left side the undistorted cubic structure is reported; on the right side the orthorombic distorted structure is shown.

The perovskite structure is quite flexible, a number of different elements can be accommodated into the A and B sites. Moreover, partial substitution of the A and B cations is possible, originating compounds like $A_{1-x}A'_xB_{1-y}B'_yO_3$.

Two of the formulations that have attracted particular attention for catalytic purposes are those of the so called LSF ($La_{1-x}Sr_xFeO_{3-\delta}$) and LSC ($La_{1-x}Sr_xCoO_{3-\delta}$) family[46]. The partial substitution of La^{3+} with Sr^{2+} decreases the global charge present on the A site and forces the metal cation in the B site to an oxidation state higher than 3+ and may at the same time create oxygen vacancies in the structure[47,48]. The total oxygen content will in this case deviate from the fully stoichiometric value of 3, and assume a variable value of $3 - \delta$, where δ indicates the nonstoichiometry value. The oxygen nonstoichiometry is specific for each oxide and depends at any time on the temperature and on the oxygen pressure surrounding the oxide. Plots of nonstoichiometry as a function of oxygen partial pressure, as illustrated in Figure 1.6, are therefore required

to map the behavior of the different oxides. It is evident from Figure 1.6 that the redox properties of the various perovskites tend to reflect the stability of the oxidation states of the B cations involved in the redox process[49]. However, enormous difference between the redox properties of the binary and ternary oxides have been reported. This is due to the fact that two factors must be taken into consideration, the crystal structure of the oxide must allow changes in composition and the transition metal must have accessible oxidation states[49]. A good example on how the crystal structure alone can influence the redox properties of a perovskite is the reduction of the cubic and the hexagonal modification of $SrMnO_3$. The initial reduction of the hexagonal modification in air occurs 600 K above the temperature for the initial reduction of the cubic $SrMnO_3$ due to a large Gibbs energy of formation of the reduced hexagonal $SrMnO_{2.5}$ compare to the cubic one[50–52].

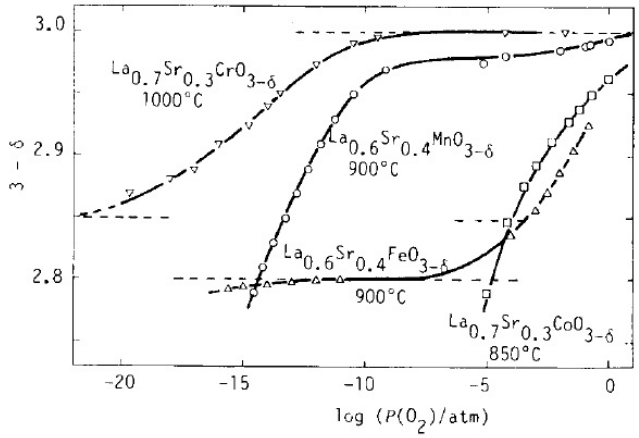

Figure 1.6: Nonstoichiometry comparison - Comparison of nonstoichiometry data of $La_{1-x}Sr_xMO_{3-\delta}$[53]

The reversible oxygen uptake and release associated with the specific nonstoichiometry range, δ, that the perovskite experiences has inspired several practical applications. One of these, and the most relevant for this PhD work, has been the reaction of this available oxygen with methane to form mixtures of CO_2, H_2O, CO and H_2[21,54–63]. Most of these works report the presence of two "types of oxygen" that respectively give rise to total

oxidation products (CO_2 and H_2O) and to selective oxidation products (CO and H_2). Several authors identified the first oxygen species as weakly bound surface oxygen and the second type as more strongly bound framework oxygen.

Maximizing the selectivity of products is a key issue in this cyclic process since total oxidation products are undesired by-products. This requires a deep understanding of the process. The focus in this PhD study has therefore been on understanding if and how the redox properties of the studied oxides influence the reaction selectivity, in order to gain guidelines for the design of new and improved oxides, for this and other related partial oxidation reactions.

2

Materials and Methods

The experimental work in this PhD study is based on the use of several characterization techniques. These techniques are briefly described in the following chapter.

Focus is set on the reasons for selecting the various techniques for this study, accompanied by a general description of each technique.

A detailed description of the different measurement parameters and equipments can be found in the experimental section of the articles that compose this PhD work.

2.1 Structural characterization

As mentioned in the introduction, one of the main requirements of the redox active materials for cyclic oxidation processes is phase stability. Therefore, particular attention has been given in this PhD study to structural characterization, both in situ and ex situ.

Several diffraction techniques were used, in all of them an X-ray or neutron beam is focused on the sample and being scattered by the atoms of the solid. From the intensity and the position of the diffracted lines (diffractograms), information about the three dimensional arrangement of the atoms in the sample is obtained.

A common data analysis tool was employed for all sets of diffraction data, the so called Rietveld method[64,65]. An approximate structure model is refined against the measured powder diffraction profile through a least-squares procedure where the residual is minimized. Unit cell dimension, atomic coordinates, site occupancies, temperature (displacement) factors and several instrument related parameters can be optimized with

the Rietveld method. The software used in this work was the GSAS/EXPGUI[66] suite of programs.

2.1.1 X-ray powder diffraction

Powder X-ray diffraction patterns were recorded with a position sensitive detector using a Siemens Bruker D5000 diffractometer and Cu $K\alpha$ 1 radiation.

By comparing the measured patterns with those reported in the Powder Diffraction File (PDF) database of the International Centre for Diffraction Data it is possible to identify which crystalline phase/phases are present in the sample. Particularly important for this type of analysis is the position of the peaks, each peak being correlated to a specific lattice plane (identified by the Miller index) and carries information about the size and shape of the unit cell. This fingerprint approach to analyses of the powder diffraction patterns helps identifying impurity phases eventually present in the samples.

In the present work, the peak position analysis was widely used to confirm the presence of the perovskite phase in the synthesized samples, and to check for presence of possible crystalline impurities at an early sample synthesis stage.

The Rietveld method was applied to the refinement of several Al doped perovskites structures studied in this PhD work.

In the case of Ceria-Zirconia based samples X-ray diffraction was also used for investigation of the average crystallite sizes of the oxidized samples (see Table 2 in Paper 2). This was performed by using the so called Scherrer equation[67] and the width of the (101) diffraction peak. Instrumental resolution was determined on the basis of a Si standard.

The Scherrer equation correlates the broadness of the diffraction peaks to the size of the measured crystals. The fact that the crystals in the sample have a finite size represents a deviation from the "perfect crystallinity", however for samples bigger than 1000 Å this effect is negligible. When the crystallites are smaller than 1000 Å this deviation becomes relevant and measurable by the broadening of the diffraction peaks.

By using the Sherrer equation (2.1), where K is the sherrer constant, α is the wavelength of the radiation, β (β_{sample}-$\beta_{standard}$) is the integral width of a reflection (in radians 2Θ) located at 2θ, the volume weighted crystallite size (D_v) can be obtained.

$$D_v = K\alpha/\beta cos\Theta \tag{2.1}$$

2.1.2 Synchrotron X-ray powder diffraction

The main disadvantage related to the use of common laboratory scale X-ray diffractometers (as described above) is that the intensity of the X-ray beam from a conventional generator is relatively low and therefore long exposure times are required, up to several hours, in order to obtain good intensities in the recorded diffractogram.

The long exposure time does not allow rapid in situ measurements, e.g. studies where the fast evolution of the crystalline structure as a function of environment changes (like temperature or atmosphere) is to be studied.

The heart of a synchrotron facility is the storage ring where charged particles travel being bent by means of magnetic fields, thereby X-rays are emitted. The energy (wavelength) of syncrotrone radiation may be tuned in a quite wide keV window, so that fluorescence issues may be avoided. The intensity of this radiation is many orders of magnitude higher than the one of conventional X-ray tubes and the data collection is therefore accomplished within a short time interval.

One of the aims of this PhD study was to evaluate the bulk stucture evolution of the oxygen carrier materials under working conditions (exposure to CH_4 and O_2 at various temperatures), synchrotron X-ray powder diffraction was, for the reasons listed above, chosen as a suitable technique for this type of studies.

In order to enable studies of the samples under working conditions a special cell (developed by Poul Norby, UiO) was used. A picture of the cell is reported in Figure 2.1.

A typical two dimensional diffractogram, as recorded with this setup, is reported in Figure 2.2, here, each line represents a reflection. The evolution of the various reflections, as gas atmosphere and temperature were varied, can be followed in this type of plots.

The powder sample was mounted inside the capillary, where a quartz pad was first inserted in order to avoid sample loss during gas flow. The inlet of the capillary was connected to the gas line through a Swage Lock ® fitting, in a similar way the outlet of the capillary was connected to a teflon line bringing the outlet gases to the ventilation.

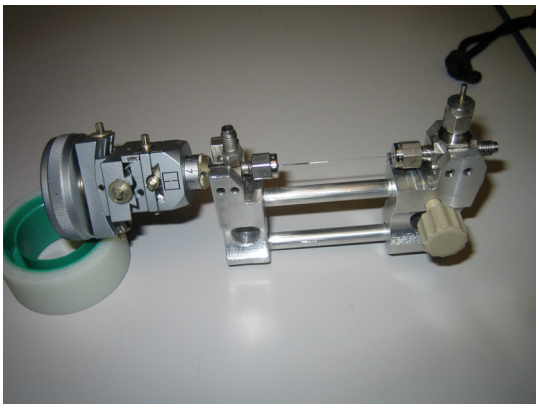

Figure 2.1: Sampe cell - Sampe cell used for in situ SXRD studies

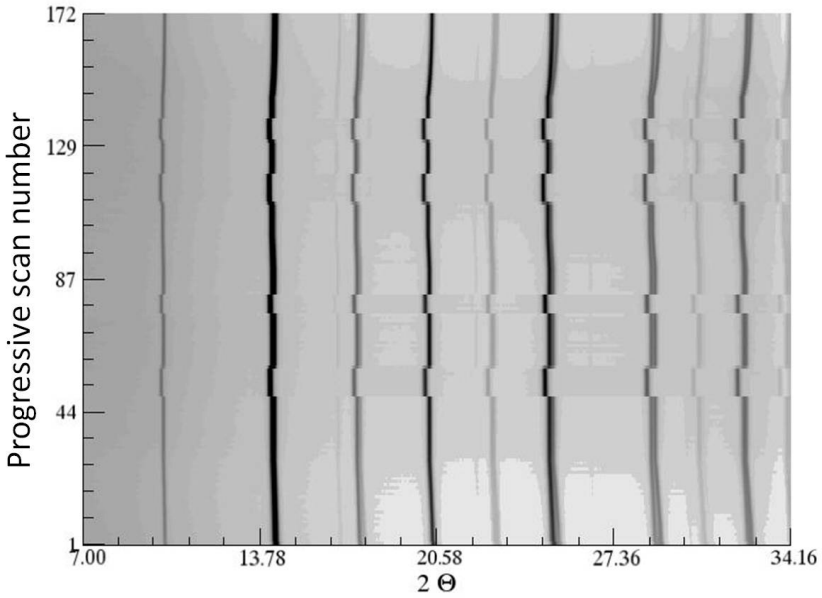

Figure 2.2: Two dimensional SXRD plot - Typical two dimensional diffractogram as recorded with the in situ cell shown in Figure 2.1

The gas flowing to the capillary was controlled and monitored through several mass flow controllers, the gas flow could be varied from the control room without stopping the experiment.

The results of this study are described in detail in paper 1 section 3.2.

2.1.3 Neutron powder diffraction

One of the limitations of X-ray diffraction techniques when studying metal oxides regards the much lower scattering of oxygen atoms compared to the metal atoms, since the photon scattering is proportional to the amount of electrons.

In neutron diffraction the scattering is due to the nuclei rather than electrons. The neutron scattering length of most atoms is similar in magnitude, however it varies quite unsistematically between the elements of the periodic table. Neutron diffraction techniques may therefore be used to detect light elements such as oxygen or hydrogen in combination with heavy atoms.

In this study neutron powder diffraction has been an essential tool in determining the oxygen content (oxygen stoichiometry) as well as the oxygen coordinates in the crystal structure, of various Al substituted perovskite oxides (at Standard temperature and pressure).

Room temperature Neutron Powder Diffraction (NPD) data were collected with PUS (Powder Universal Spectrometer) two-axis diffractometer at the JEEP-II reactor at Kjeller, Norway. Data were collected over a 2 θ range of 10° to 130° using neutrons of wavelength 1.5561 Åand rebinned into steps of 0.05 degrees.

Rietveld refinements of the NPD data were performed using the GSAS/EXPGUI[66] suite of programs.

2.2 Activity characterization

2.2.1 Catalytic tests

A main focus of this PhD work has been to reveal the mechanism of the reaction between methane and the various reducible metal oxides. In order to study the reaction a SSITKA setup (Steady state isotopic transient kinetic analysis setup) has been adapted to the target reaction. A schematic representation of this setup is shown in Figure 2.3.

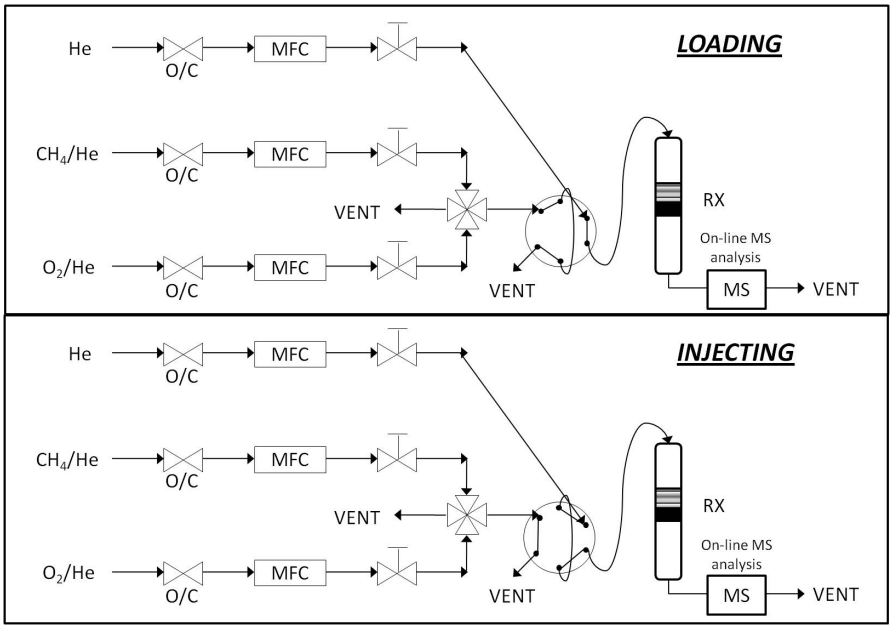

Figure 2.3: - Experimental setup used during pulse experiments

The reaction between methane and the reducible oxides occurs in a short time window. Since the framework oxygen of the oxides is consumed during the reaction, this makes an accurate quantification of the reaction products, over the entire reaction time, quite challenging in a continuous feed setup. For this reason, in accordance with previous reports on similar studies[68,69], a pulse setup system was chosen.

As can be seen in Figure 2.3 a four way valve was used to switch between the premixed 10% CH_4 in Helium and 10% O_2 in Helium. The selected gas from the four way valve was sent (in loading position) through the 0.25 ml loop in the six way valve. At the same time, an independent line was used to continously send the carrier gas (Helium) to the reactor through the six way valve. When the six way valve was switched from loading to injection the carrier gas was forced to flow through the loop and take the discrete amount of gas (1.04 μmol, either 10% CH_4 or 10% O_2) contained in the loop to the reactor. The reactor, a classical plug flow reactor, is illustrated in Figure 2.4

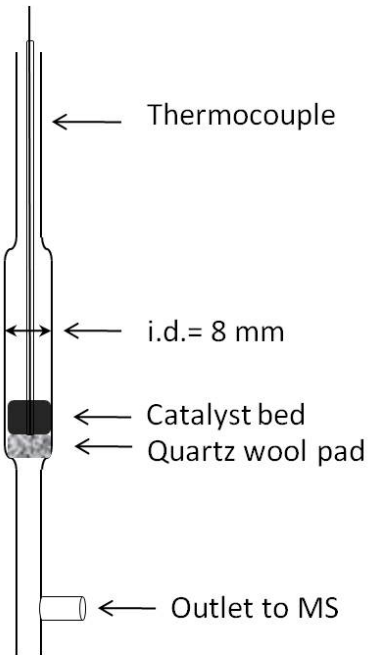

Figure 2.4: - Schematic reactor illustration

The four and the six way valve, as well as the oven and all mass flow controllers were controlled by using a LabVIEW software interface.

The mass spectrometer (Pfeiffer Omnistar, MS) was connected directly below the catalyst bed (Figure 2.4) to avoid loss in definition of the signal shape due to back mixing of gases. A typical illustration of raw data output registered from the MS is reported in Figure 2.5.

The carrier gas signal is not reported in Figure 2.5 for graphical reasons. As can be noticed each gas pulse appears as a line in the overall data figure, and as a well defined peak in the zoomed inlet. A calibration of the setup was performed routinely, this was done by sending, 10-20 pulses of the relevant gases (CH_4, O_2, CO_2, CO, H_2) one by one to the reactor loaded with quartz and heated to the test temperature. The area under each peak was integrated and used as calibration for quantification of these gas species during the following tests. All responses were normalized with the signal from the carrier gas. Since no H_2O calibration was performed, the quantification of this specie was derived from the H_2 balance.

The data treatment during catalytic tests was performed by integrating each single peak from each single m/z recorded by the MS. The integrated areas were then divided by the calibration values and a μmol value was obtained for each gas species in each gas pulse. These values were then used to calculate CH_4 conversion:

$$CH_4\ conversion\% = 100 \times \frac{p(CH_4)_{in} - p(CH_4)_{out}}{p(CH_4)_{in}}$$

and CO and H_2 selectivity:

$$CO\ selectivity\% = 100 \times \frac{p(CO)_{out}}{p(CO)_{out} + p(CO_2)_{out}}$$

$$H_2\ selectivity\% = 100 \times \frac{p(H_2)_{out}}{2 * p(CH_4)_{in} - p(CH_4)_{out}}$$

For each pulse, carbon balance was calculated as the sum of unconverted CH_4, CO_2 and CO.

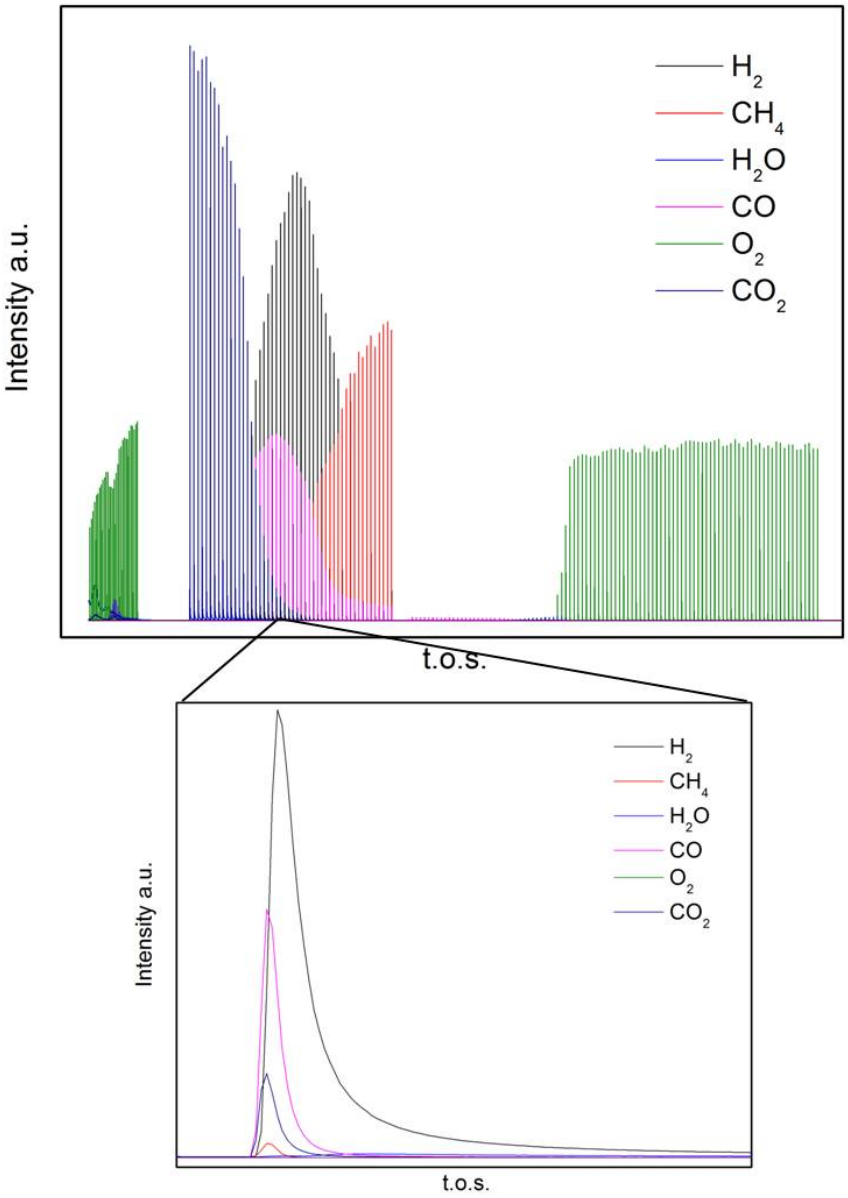

Figure 2.5: - Typical MS raw data output from a pulse test

2.2.1.1 Isotopic labeling catalytic tests

Isotopic labeling catalytic experiments are a powerful tool that may give an unambiguous answer to crucial catalytic issues. Isotopically labeled molecules behave chemically exactly like unlabeled molecules (except for H/D exchange), therefore, by analyzing the distribution of the labeled atoms at the exit of the reactor, precious insight into relative reaction rates involving molecules in the reactor can be gained.

In the present work discrete pulses of a mixture of ^{13}C labeled CH_4 and ^{12}CO were reacted with the materials of interest. A setup very similar to the one described in Figure 2.3 was used, in this case an additional MFC (Mass flow controller) was used beside the one dedicated to CH_4 (where ^{13}C labeled CH_4 was now flowing) in order to feed CO.

The calibration, the test setup and the data treatment were carried out in a similar way as described in section 2.2.1. ^{13}C labeled CH_4, was included in the calibration. Several m/z values were recorded with the Mass Spectrometer (2, 4, 12, 13, 14, 15, 16, 17, 18, 28, 29, 44, 45) in order to monitor all possible ^{13}C labeled reactants and products. CO selectivity and CH_4 conversion were calculated as described above.

In addition to the standard data treatment, special attention was given in these type of tests to the ^{13}C distribution in the unreacted CH_4 and in CO and CO_2. The statistical $^{13}C/^{12}C$ distribution in the products was calculated as

$$\frac{p(^{13}CH_4)_{in} * CH_4 conversion * 0,01}{p(^{12}CO)_{in} - p(^{13}CH_4)_{out}/p(^{12}CO)_{in}}$$

and compared to the $^{13}C/^{12}C$ distribution in CO and CO_2.

Back formation of CH_4 was assessed from the $^{13}C/^{12}C$ ratio in effluent CH_4.

2.3 Oxygen nonstoichiometry

Particular focus has been given in this PhD work to the assessment of the oxygen nonstoichiometry of the various oxides under the various studied conditions.

Different analytic techniques have been employed depending on the target conditions, below follows brief descriptions.

2.3.1 Cerimetric titration

Cerimetric titration[70] was used to derive the oxygen content of the Al substituted perovskite oxides at room temperature and ambient pressure.

This titration is based on the dissolution of the sample in acidic solution and subsequent reduction of the high valent species (Fe^{4+} and Co^{3+}) by a reductant. In order to avoid oxidation of the reductant by the oxygen dissolved in the acidic solution, this was removed by Ar bubbling prior to reductant dissolution. For the same reason, the titration was performed in a air tight vessel under Ar bubbling.

A precise excess amount of high purity ammonium iron (II) sulfate salt (Mohr's salt, reductant) was dissolved in aqueous 1M HCl solution. The sample was then digested in this solution (up to 48 hours). During this step iron (II) from the Mohr's salt was oxidized from Co^{3+} and Fe^{4+} (if present), as indicated in the reactions below. Fe^{3+} and Al^{3+} do not take part in the redox reaction.

$$Co^{3+} + Fe^{2+} \rightarrow Co^{2+} + Fe^{3+}$$

$$Fe^{4+} + Fe^{2+} \rightarrow 2Fe^{3+}$$

The remaining Fe^{2+} was then titrated with a solution of Ce^{4+} in the presence of a Fe(II) 1,10-phenanthroline complex (Ferroin) as indicator. The amount of Fe^{4+}, and therefore the oxygen stoichiometry, could be extrapolated.

2.3.2 Thermogravimetric analysis

Thermogravimetric analysis was used in 2 types of experiments.

In the first case, the oxygen content of the various Al substituted perovskite oxides at 873 K was measured. The results of these experiment are reported in paper 3. The sample, about 50 mg, was loaded in the Thermogravimetric balance (PerkinElmer, Pyris 1 TGA) where synthetic air was flowing (20 Sml/min), heated slowly (1 K/min) to 1073 K and cooled down to room temperature. During this procedure possible surface contaminations were removed. This step was repeated until a stable weight value was reached at RT before and after the thermal treatment. The sample was then directly heated to 873 K at 5 K/min. The weight change was then converted into

oxygen loss and thereafter oxygen nonstoichiometry, the data in this form are reported in the article.

The second sets of experiment based on thermogravimetric analysis was performed at SINTEF Materials and Chemistry (Oslo, Norway).The TG equipment used in this case (SETARAM Setys Evolution TGA) was equipped with an in-house gas mixing system and oxygen sensor. In this experiments the weight variation was measured as a function of pO_2. The weight variation was then related to the oxygen nonstoichiometry variation and the data in this form are reported in paper 1.

2.3.3 Flowing titration

The relationship between the oxygen nonstoichiometry and the partial pressure of oxygen was further measured by a method similar to that reported by Kim and coworkers[44]. The principle is that a defined amount of sample is exposed to a premixed gas mixture characterized by a specific pO_2 for several hours, so that equilibrium between the sample and the gas mixture is obtained. The sample is then exposed to air flow, the amount of oxygen adsorbed from the sample during exposure to air is measured and from this number the oxygen nonstoichiometry in equilibrium with the previous pO_2 is found.

The setup used in the pulse tests and described in Figure 2.3 was modified and adapted to the flowing titration experiment. A schematic description of the setup is reported in Figure 2.6.

As can be seen, He, CO_2 and H_2 were mixed to establish the various pO_2. This was realized through the following equilibria:

$$CO_2 \leftrightarrow CO + \frac{1}{2}O_2$$

$$pO_2 = \left(K_{eq1}\frac{pCO_2}{pCO}\right)^2$$

$$H_2O \leftrightarrow H_2 + \frac{1}{2}O_2$$

$$pO_2 = \left(K_{eq2}\frac{pH_2O}{pH_2}\right)^2$$

The software "HSC chemistry" was used as a tool to calculate the pO_2 of the different gas mixtures.

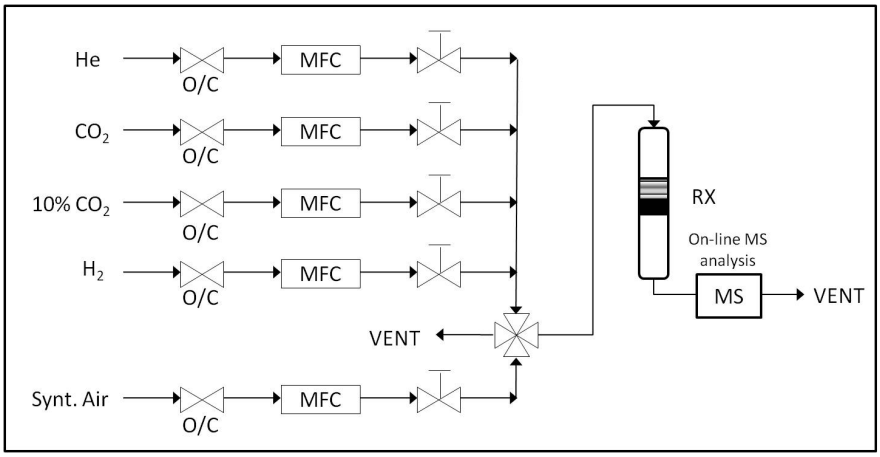

Figure 2.6: - Experimental setup used during pulse flowing titration

The mass flow controllers were remotely programmed so that the various gas mixtures could be run automatically, following a programmed schedule for the whole experiment.

The sample (0.3-1 g) was loaded in the reactor illustrated in Figure 2.4 and heated to 873 K in air. Thereafter the first gas mixture (total gas flow 30 ml/min) was sent through the sample, for 3 hours. After these 3 hours the reactor was flushed with He (AGA 99.9995 %, 90 ml/min) for 30 min, and finally dry air was fed to the reactor (5 ml/min).

The effluent gases were monitored by an on line mass spectrometer (as previously described), recording the mass numbers (m/z) 4, 14, 18, 28, 32 and 44.

A typical example of MS raw data output at the end of an experiment can be seen in Figure 2.7.

In some of the tests carbon deposition during the exposure to the CO_2/H_2/He mixtures took place. This was observed as small amounts of CO_2 released immediately after exposure to air. In these cases, quantification of the amount of oxygen consumed during the CO_2 formation was performed, and this value was subtracted from the total oxygen absorbed.

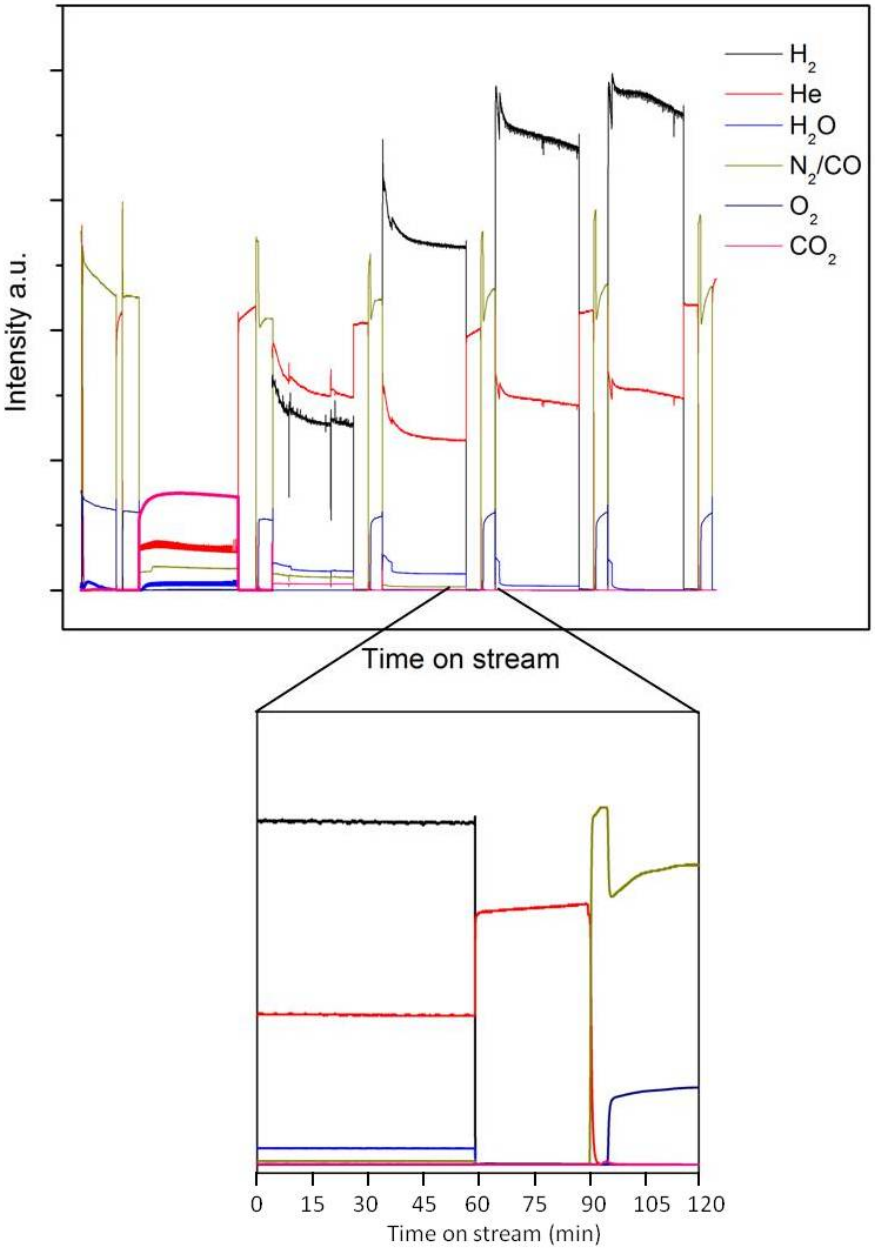

Figure 2.7: - Typical flowing titration Mass spectrometry raw data output

2.4 Additional characterization

Some of the data collected in this PhD work are the results of collaborations with other research groups. In this case the data collection work was not entirely performed by the author.

The neutron powder diffraction data were collected at IFE (Institute for Energy Technology, Kjeller, Norway), the data treatment was performed by the author.

The thermogravimetric measurements, and the respective data analysis, at variable pO_2 described in section 2.3.2 was performed by Dr Egil Bakken at Sintef Materials and Chemistry (Oslo, Norway).

The TEM measurements described in the third paper have been entirely performed by Dr Yanjun Li at Sintef Materials and Chemistry (Trondheim, Norway).

The XPS data included in the third paper have been collected by Dr Spyridon Diplas and Martin Sunding Fleissner, the data analysis has been performed by the author in collaboration with Dr Spyridon Diplas. The detailed experimental description for this last two techniques can be found in the third paper.

3

Synopsis of Results

This chapter contains a brief overview of the main findings of this study.

The detailed results obtained during this PhD, together with their discussion, are summarized in the three articles included at the end of the thesis.

The starting point of this study was the need for a non conventional, alternative, process to produce syngas from natural gas in offshore installations. Several literature reports had been published, where the use of framework oxygen of reducible oxides in direct contact with methane was presented as an option.[21,54–59,61,62,68,69,71–74].

However none of these reports were able to answer the question on how selectivity towards syngas could be optimized, and most of all, how and why the structure and the composition of the reducible oxides influenced the reaction.

In order to provide the answers to these challenging questions a multidisciplinary approach was chosen, where, classical catalytic methods were combined with typical structural inorganic chemistry techniques.

This double approach led to the discovery of the strong influence of the thermodynamics of the oxides on the surface reaction and this connection forms the basis for a main achievement of this PhD work.

3.1 Structural studies

Two main families of reducible oxides were studied in this PhD work, cerium oxide based oxides and lanthanum ferrite based oxides.

3.1.1 Ceria based oxides

In the first case, materials well known from literature were used, pure CeO_2 and $Ce_xZr_{1-x}O_{2-\delta}$ (x=0.25, 0.5 and 0.75). The oxides were impregnated with Pt in order to increase the reactivity towards methane.

These materials are widely studied in literature. Therefore the structural studies, in this case, were limited to powder XRD analysis and more thorough investigations were found to be beyond the scope of this work.

The results obtained from the XRD analysis are reported in paper 2 and in Figure 1.3, as can be seen the materials synthesized in this work obey the Vegard's law, in agreement with similar materials previously reported in literature.

3.1.2 Perovskite based oxides

Several of the perovskite based samples synthesized in this PhD study had not been reported in the literature. For this reason a deeper structural characterization work was performed on this second class of studied materials.

The starting oxide $La_{0.8}Sr_{0.2}Fe_{0.8}Co_{0.2}O_{3-\delta}$, and the ones that were developed following this starting stoichiometry, were analyzed with powder XRD, syncrotron powder XRD and neutron diffraction. The advantages of the different techniques were discussed in section 2.1.

The starting perovskite material that was tested in this PhD work, $La_{0.8}Sr_{0.2}Fe_{0.8}Co_{0.2}O_{3-\delta}$ had been previously reported in literature[75]. The addition of small amount of Rh in a post synthesis step, as expected, did not influence the bulk structure of the oxide.

Metal oxides supported on inert high surface area materials (as for example γ-alumina or silica) are very common catalysts. This methodology was applied to the perovskite based materials and the sample reported in paper 1, named LSFCB is the results of a "supported oxide" inspired synthesis. Boehmite, an aluminium oxide hydroxide mineral ($\gamma-AlO(OH)$) was introduced in the synthesis of $La_{0.8}Sr_{0.2}Fe_{0.8}Co_{0.2}O_{3-\delta}$ and the sample that resulted is presented in paper 1.

The XRD analysis revealed the presence of multiple phases in the sample (as expected upon addition of boehmite) but they could not be simply assigned to the original $La_{0.8}Sr_{0.2}Fe_{0.8}Co_{0.2}O_{3-\delta}$ and the aluminium oxide hydroxide, a reaction between

the two materials had occurred and in order to determine the products of this reaction synchrotrone X-ray powder diffraction was used.

The structural analysis of this sample is reported in paper 1, briefly, analysis of the diffractograms revealed the formation of a solid solution perovskite phase with Al partially present together with Fe and Co in the B site. In addition two more crystalline phases were identified in the sample, a hexaaluminate type oxide ($LaFeAl_{11}O_{19}$) and a spinel Fe/Al mixed oxide.

The exact stoichiometry of the new perovskite was found with Rietveld analysis, and this inspired the synthesis of this oxide in a phase pure form. This oxide is presented in paper 1 under the name of LSFCA.

The catalytic results obtained from these three oxides inspired the synthesis of a series of Al substituted perovskites as the one reported in paper 1, with variable Al amounts in the B site of the oxide (10%, 25%, 40% and 60%). Several stoichiometries were synthesized and those samples form the basis of results presented in paper 3.

The incorporation of Al in the B site of $La_{0.8}Sr_{0.2}Fe_{0.8}Co_{0.2}O_{3-\delta}$ had several consequence on the structure of the oxide itself.

Laboratory scale XRD gave indications that all Al substituted samples were synthesized as phase pure materials, and that the unit cell was changing continuously as a function of Al substitution level. However, space group identification and oxygen stoichiometry could not be assessed by lab scale powder XRD, all these samples were therefore measured with neutron powder diffraction.

The structure analysis of the neutron powder diffractograms revealed that all the samples took rhombohedral symmetry (space group $R\bar{3}c$, all refined unit cell values are given in table 1, paper 3) and that the oxygen content was very close to 3. NPD also confirmed that no additional phases were present in any of the samples.

The difference in ionic radius between Al^{3+} and Fe^{3+} and Co^{3+} give rise to a decrease in unit cell dimension upon Al substitution. At the same time a better "match" between the size of the A site and B site was achieved upon increasing Al content, therefore the perovskite tolerance factor approached 1, the tilt angle between the octahedras forming the perovskite structure decreased and the unit cell approached the ideal perovskite cubic symmetry as can be seen in figure 3.3.

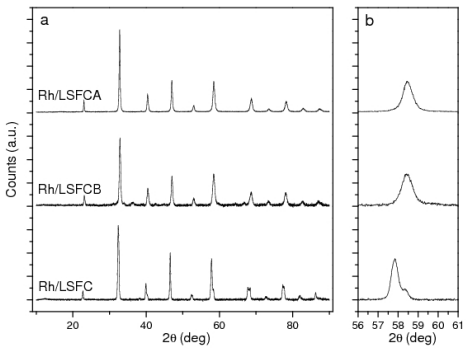

Figure 3.1: X-Ray diffraction patterns Paper 1 - (a) Powder X-Ray diffraction patterns for the samples studied in Paper 1.

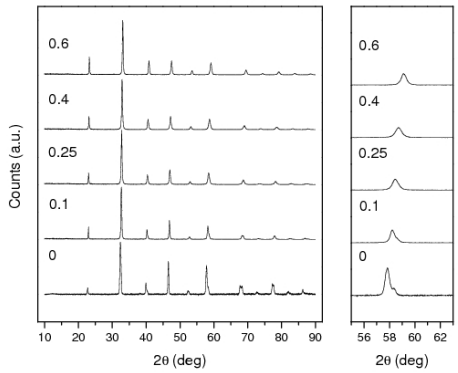

Figure 3.2: X-Ray diffraction patterns Paper 3 - Powder X-Ray diffraction patterns for the samples studied in paper 3.

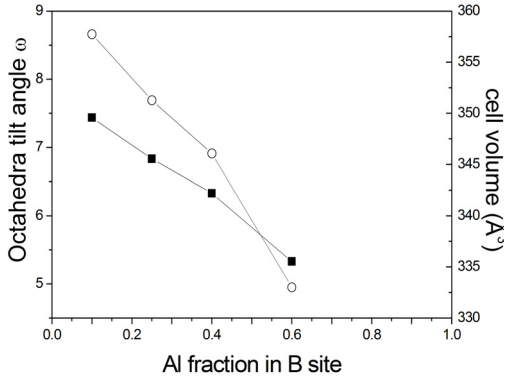

Figure 3.3: Al influence on unit cell - Influence of Al content on the unit cell size and tilt angle

3.2 Oxygen nonstoichiometry studies

A central point of this PhD work is the framework oxygen of the various oxides as a key reactant. The oxygen content of reducible metal oxides depends on the temperature and oxygen partial pressure. It was therefore crucial to map the oxygen content of the oxides as a function of the oxygen partial pressure at the reaction temperature, as indicated by the following equation.

$$MO_y \Leftrightarrow \frac{1}{2}xO_2 + MO_{y-x} \tag{3.1}$$

Different methods were employed, as described in section 2.3.

These type of measurements define the equilibrium oxygen content, and are widely used in thermodynamics studies, however very few catalytic studies investigate this properties, probably because "equilibrium" is often far from what catalysis investigates.

3.2.1 Ceria based oxides

The data collected for the ceria based oxides were inspired by similar studies reported in literature[44,76,77], and the results obtained were in agreement with these works. As can be seen in Figure 3.4 the ratio between oxygen and cerium (which indicates the degree of reduction, $Ce^{4+} + e^- \Leftrightarrow Ce^{3+}$) decreases with decreasing pO_2 for each sample. The

observed trend is expected from thermodynamic principles. Importantly, the presence of Zr in the solid solutions increases the amount of reduced Ce atoms at a given pO_2.

The equilibrium constant for oxidation of a metal oxide, such as CeO_{2-x}, is directly related to pO_2 given that the activities of solid phases are one. From these measurements, therefore, the equilibrium constant and the Gibbs Free Energy, ΔG, for the reduction reaction could be derived. ΔG for the reduction reaction is reported in figure 3.4, upper abscissa.

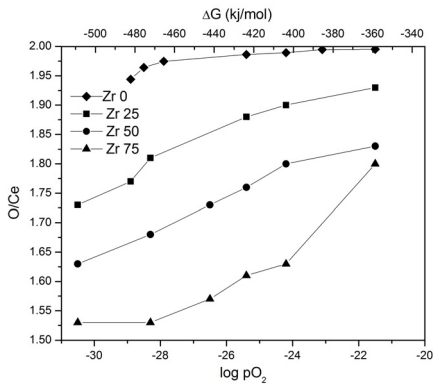

Figure 3.4: Nonstoichiometry in Ceria based oxides - O/Ce ratio and ΔG oxidation as a function of pO_2 in ceria-zirconia solid solutions at 873 K

The enhanced reducibility of Ce^{4+} atoms in solid solutions with Zr have been related in the literature to the number of ways oxygen can be removed from localized clusters (localized entropy effects). Studies of enthalpy and entropy of reduction showed that enthalpy of reduction of solid solutions was significantly lower than in pure CeO_2 but independent on the Zr substitution level (for Zr subsitution level higher than 10%). At the same time the entropy of reduction changed with composition and Zr amount.

3.2.2 Perovskite based oxides

The relationship between oxygen stoichiometry and oxygen partial pressure for most of the perovskite oxides studied in this PhD work was investigated (the perovskite synthesized with boehmite was not included in this type of investigation due to its multiphase nature). The chemical reaction in this case can be generally written as:

$$ABO_3 \Leftrightarrow \frac{1}{2}xO_2 + ABO_{3-x} \tag{3.2}$$

Some perovskite based oxides are easily reduced even at low temperatures[78]. For this reason full stoichiometry in air atmosphere at 873 K could not be assumed. The oxygen stoichiometry in air atmosphere at 873 K was therefore measured.

Oxygen nonstoichiometry at room temperature (air atmosphere) was measured by neutron powder diffraction and cerimetric titration and both techniques returned values very close to zero.

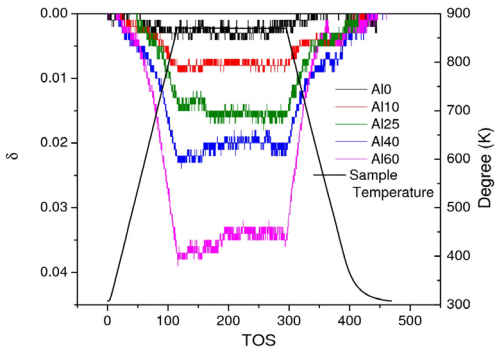

Figure 3.5: Oxygen nonstoichiometry, TG measurements - Oxygen nonstoichiometry as a function of temperature as reported in paper 3.

The thermogravimetric measurements of the samples in air atmosphere, Figure 3.5, revealed that the oxygen nonstoichiometry increases with the Al content at a given temperature. The oxygen nonstoichiometry value at 873 K in air atmosphere was extrapolated from these measurments.

The results of the flowing titration performed at 873 K are reported in paper 3 and in Figures 3.6 and 3.7. The oxygen nonstoichiometry is affected by the introduction of Al, but no systematic correlation with the amount of Al substitution could be found. Oxygen content variations as a function of pO_2 are less marked in the samples with the highest Al content. It is important to remember that Al, just like Zr, is not reducible upon pO_2 variations, the variation in oxygen content in the oxides is therefore linked to the decrease in oxidation state of Fe and Co. The relative amount of Fe and Co will

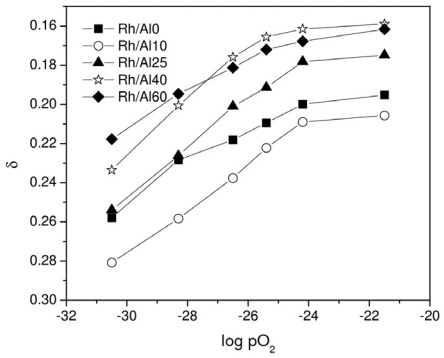

Figure 3.6: Flowing titration perovskites - Oxygen nonstoichiometry as a function of pO_2 for the Al substituted perovskite oxides, from paper 3

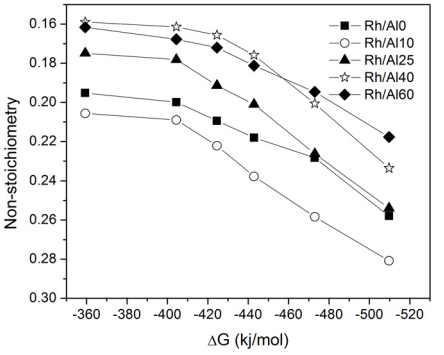

Figure 3.7: ΔG oxidation perovskites - ΔG of oxidation for the various perovskite oxides studied in paper 3 at the different pO_2

decrease upon increase in Al content, therefore an alternative picture of the state of the oxides is given by the Fe and Co average oxidation state as a function of pO_2 as reported in paper 3, table 2.

Up to moderate Al substitution levels (40 %) the oxidation state of Fe and Co tends to be higher for higher Al contents, the situation is reversed at even higher Al amounts (60 %), where lower oxidation states are obtained for Fe and Co.

3.3 Catalytic studies

Catalytic studies, performed by the techniques described in section 2.2, have been the core of this PhD work.

Results from the CH_4 transient experiments are reported in the three articles that form this thesis, while isotopic labeling studies are reported in the last two articles. In this section only a brief overview of these findings is presented.

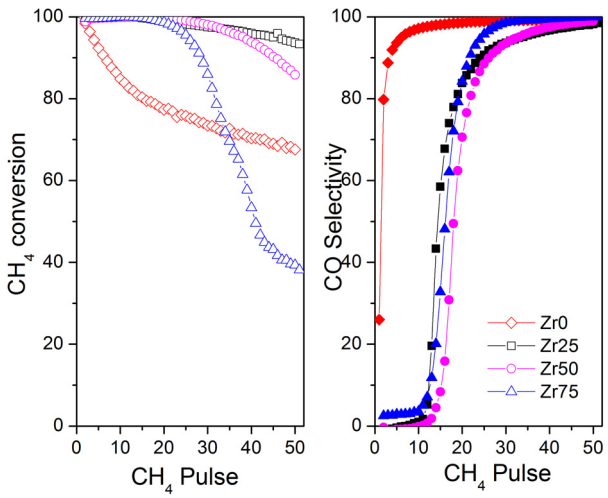

Figure 3.8: Pulse test Ceria based materials - CH_4 conversion (empty markers) and CO selectivity (full markers) as a function of CH_4 pulse number.

Methane conversion showed two different patterns for the Pt/ceria based and the Rh/perovskite based samples. In the ceria case the conversion started for all the solid

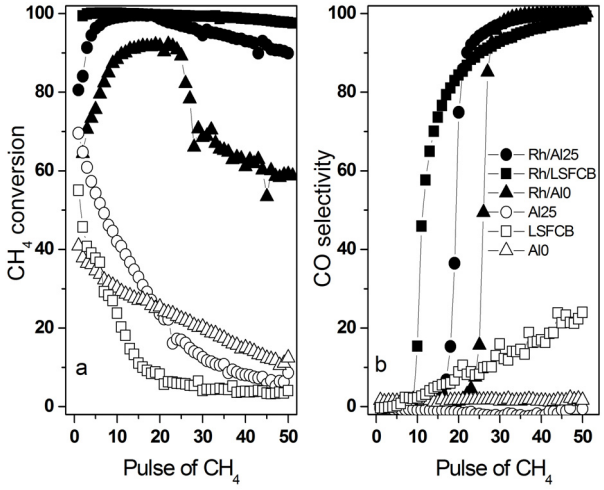

Figure 3.9: Pulse test Perovskite based materials from Paper 1 - CH_4 conversion and CO selectivity as a function of CH_4 pulse number.

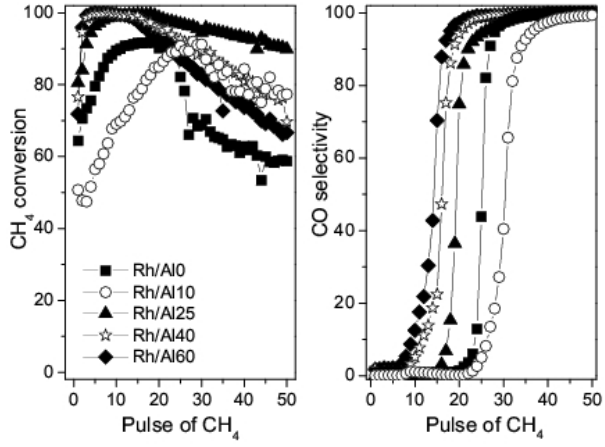

Figure 3.10: Pulse test Perovskite based materials from Paper 3 - CH_4 conversion and CO selectivity as a function of CH_4 pulse number.

solutions at values close to 100 % and decreased with the pulse number, whereas in the perovskite based samples the conversion increased with pulse number and went through a maximum before it dropped.

A common trend observed in all perovksite based oxides impregnated with Rh is that the selectivity always increased with the pulse number. It usually started from values close to zero (bulk ceria is an exception) and rapidly increased to values close to 100 % once it passed a "critical pulse number".

This selectivity pattern has also been observed in most of the literature reports regarding direct methane conversion with framework oxygen. The various literature hypothesis are extensively discussed in the three articles that form this thesis.

A similar trend between catalytic and equilibrium nonstoichiometry results, reported in the previous section, was noticed for both ceria and perovskite based materials. Indeed the reaction between methane and the metal oxides, once hydrogen is released (either as molecular hydrogen or as water), leaves a surface carbon atom that faces three possibilities:

- Deposition on the surface of the oxide as carbonaceous deposit (coke) until oxygen is introduced in the system
- Combination with one oxygen atom from the framework of the oxide and release as CO
- Combination with one oxygen atom from the framework of the oxide and further reaction with another oxygen atom from the framework of the oxide before release as CO_2

In our data we do observe that all these three options took place; at the beginning of the test (high oxygen content) CO_2 was released, when a critical nonstoichiometry value was reached, CO was the main product and as most oxygen was released from the oxide, coke deposition started to build up (as evident from C balance measurements). Combination of the carbon atom with one oxygen atom from the framework of the oxide and further reaction with another oxygen atom from the framework of the oxide before being released as CO_2 can be described as:

$$xCO + MO_y \Leftrightarrow xCO_2 + MO_{y-x} \tag{3.3}$$

This reaction can further be divided in:

$$MO_y \Leftrightarrow \frac{x}{2}O_2 + MO_{y-x} \tag{3.4}$$

and

$$xCO + \frac{x}{2}O_2 \Leftrightarrow xCO_2 \tag{3.5}$$

Equation 3.4 is the reaction that has been studied in the previous section, and the ΔG of reaction have been measured for several x values. As can be noticed in Figure 3.4 and 3.7 the ΔG of oxidation becomes more and more negative as the nonstoichiometry increases. Equation 3.5 is simply the oxidation of carbon monoxide, and the ΔG for this reaction is found in the NIST database[79].

By summing the ΔG for these two reactions, for the different oxides and the various nonstoichiometry values, the global ΔG (equation 3.3) can be found for each nonstoichiometry measured in the flowing titration. From these ΔG values, the K_{eq} for the reaction 3.3 as a function of nonstoichiometry can be found. Thereafter, the CO/CO_2 ratio as a function of nonstoichiometry can be calculated.

Finally it was accomplished to estimate the CO/CO_2 ratio, at equilibrium, over the various oxides, at the various nonstoichiometry values.

When the CO/CO_2 couple was at equilibrium with the oxides during the methane pulses, the measured CO selectivities were in agreement with the equilibrium values predicted as described above.

This was indeed the case for all the studied samples, both ceria based and perovskite based, as described in the respective articles.

3.3.1 Isotopic labeling studies

The data described in the previous section suggested equilibrium between CO and CO_2 during the reaction between methane and the studied oxides. As will be shown below, isotopic labeling studies confirmed this conclusion.

If thermodynamic equilibrium is achieved in the system, when sending discrete pulses of a mixture of ^{13}C labeled CH_4 and ^{12}C CO then the ratio between $^{13}CO/^{12}CO$ and $^{13}CO_2/^{12}CO_2$ should correspond to the statistical $^{13}C/^{12}C$.

This was indeed the result obtained from the catalytic test of the selected samples, as reported in Figure 3.11 (in the case of ceria based oxides) and Figure 3.12 (in the case of perovskite based oxides).

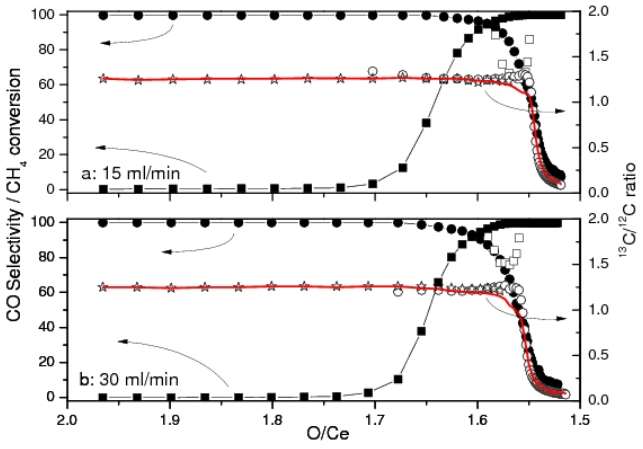

Figure 3.11: Isotopic labeling studies ceria - CH_4 conversion (circle), CO selectivity (square) and statistical $^{13}C/^{12}C$ ratio(solid line), together with $^{13}CH_4/^{12}CH_4$ (square), $^{13}CO/^{12}CO$ (circle) and $^{13}CO_2/^{12}CO_2$ (star)as a function of O/Ce over $Pt/25CeZrO_2$.

3.4 Surface analysis

The results that were obtained during the years of work on this PhD project, pointed progressively towards an important influence of the bulk phase, over possible surface implications. Bulk characterization techniques, such as for example XRD, thermogravimetric analysis and nonstoichiometry measurements were given more focus than surface characterization such as XPS and TEM/SEM.

Nevertheless, many questions about the influence of surface on the observed phenomena arose during this work, and an extensive surface characterization work, especially on the perovskite based samples was performed. The relevant results related to these studies are included in paper 3.

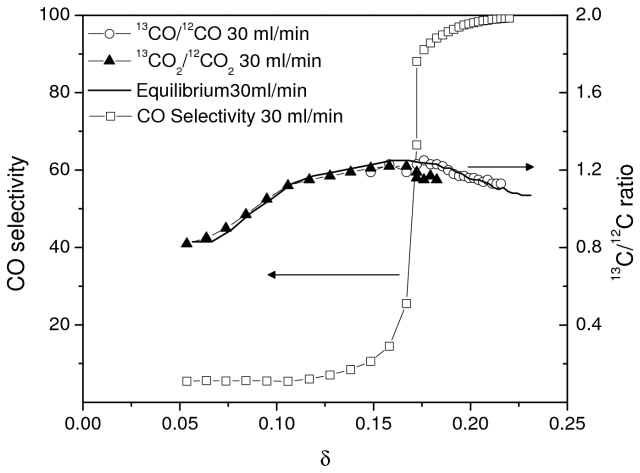

Figure 3.12: Isotopic labeling studies perovskites - CO selectivity, statistical $^{13}C/^{12}C$ ratio, together with $^{13}CO/^{12}CO$ and $^{13}CO_2/^{12}CO_2$ as a function of non stoichiometry over Rh/25Al at 873 K

No further details about the TEM work will be included in this introduction since the author was not involved in the data analysis process.

A few words about the XPS study need to be spent. X-Ray photoelectron spectroscopy is a powerful technique that allows investigations of the chemical state of the surface of a material, both quantitatively and qualitatively. In the present study the chemical state of the reducible elements before and after reduction with methane, as well as their relative amount, was of high interest. The perovskite characterized by 25 % Al substitution in the B site was therefore carefully analyzed with this technique. The most relevant results, with some comments are reported in this section. These and more results obtained from this study as well as their discussion can be found in paper 3.

The pretreatment chamber of the XPS instrument allowed samples to be alternatively exposed to methane and air at 773 and 973 K, and thereafter cooled down and measured without exposure to air.

The oxidation state of Rh, in the as synthesized samples, after reduction in methane and after reoxidation in oxygen, respectively, at 773 K was determined. The position of the Rh 3d peak for the as prepared and the reoxidized sample was very similar, and typical for Rh_2O_3 (see paper 3 for more details). The peak position for the reduced sample was shifted towards lower binding energy, confirming the formation of metallic rhodium. The intensity of the Rh peak was much higher in the as prepared samples, compared to the reduced and reoxidized samples, this can be due to several phenomena as for example diffusion of Rh species into the bulk of the sample or coverage of the Rh particles by carbon species. A final answer on this point calls for the use of either complementary techniques (as for example environmental TEM) or reference oxide systems to be measured prior to the sample.

The oxidation state of Fe and Co under the listed experimental conditions was of great interest. The distinction between metallic, bivalent and trivalent Fe and Co species by XPS is a challenging task, especially when more oxidation states could be present simultaneously. No distinct peaks for the three oxidation states were observable, this is due to the small shift in the peak position between the three oxidation states. Chemical analysis relies therefore often on peak broadening and shoulders effects. A detailed analysis of these spectra is reported in the paper 3.

3. SYNOPSIS OF RESULTS

Is the author opinion that the use of XPS to determine oxydation state of the various element present in such complex perovskite samples, before and after reaction with methane, should rely on a sound characterization work on simple model samples. The surface analysis of these model samples, under exposure to methane and oxygen, can then be used as starting point for the data analysis of the complex oxides.

4

Conclusions

The present PhD study has provided a deeper understanding of the reaction mechanism between methane and noble metal impregnated reducible oxides into partial (CO, H_2) and total (CO_2, H_2O) oxidation products.

Two selectivity behaviours, for CO and H_2, during the reaction were identified:

- low selectivity zone in the first part of the reaction
- high selectivity zone in the second part of the reaction

This selectivity pattern was found to be related to the equilibrium redox properties of the relative oxides.

The redox properties of the studied oxides were tuned by tailoring the stoichiometry. For this purpose Ce was substituted with Zr in Pt/CeO_2 and Fe and Co were substituted with Al in $La_{0.8}Sr_{0.2}Fe_{0.8}Co_{0.2}O_{3-\delta}$.

Variation in reaction selectivity was indeed shown as a consequence of stoichiometry tailoring.

Isotopic labeling studies showed total scrambling of ^{13}C between CO_2 and CO confirming thermodynamic equilibrium between these two species.

All the presented perovskite based oxides were characterized by rhombohedral symmetry (space group $R\bar{3}c$). Substitution of Fe and Co with Al resulted in smaller unit cell, and less octahedral tilting.

Structural stability of the Rh impregnated perovskite sample ($La_{0.8}Sr_{0.2}Fe_{0.8}Co_{0.2}O_{3-\delta}$), as well as of the 25 % Al substituted perovskite sample, was demonstrated by means of in situ synchrotron X-ray diffraction.

References

[1] Agency, I. E. Technical report, IEA, (2010).

[2] Mokrani, T. and Scurrell, M. *Catalysis Reviews-Science and Engineering* **51**(1), 1–145 (2009).

[3] Diepen, J. A. M. M. M. A. V. *Chemical Process Technology*. Wiley, (2001).

[4] Seier, H. and Emig, G. *Divided Catalytic Processes*. Springer, (2004).

[5] Bennett, C. O., Werner O. Haag, B. C. G., and Knzinger, H. In *Advances in Catalysis*, volume Volume 44, 329–416. Academic Press (1999). 0360-0564 doi: DOI: 10.1016/S0360-0564(08)60515-5.

[6] Silveston, P., Hudgins, R. R., and Renken, A. **25**(2), 91–112 (1995). 0920-5861 doi: DOI: 10.1016/0920-5861(95)00101-K.

[7] Herguido, J., Menndez, M., and Santamara, J. *Catalysis Today* **100**(1-2), 181–189 (2005).

[8] Ramos, R., Herguido, J., Menendez, M., and Santamaria, J. *Journal of Catalysis* **163**(1), 218–221 (1996).

[9] Creaser, D., Andersson, B., Hudgins, R. R., and Silveston, P. L. *Chemical Engineering Science* **54**(20), 4437–4448 (1999).

[10] Rubio, O., Herguido, J., and Menendez, A. *Applied Catalysis a-General* **272**(1-2), 321–327 (2004).

[11] Sloczynski, J. *Applied Catalysis a-General* **146**(2), 401–423 (1996).

[12] Creaser, D., Andersson, B., Hudgins, R. R., and Silveston, P. L. *Journal of Catalysis* **182**(1), 264–269 (1999).

[13] Creaser, D., Andersson, B., Hudgins, R. R., and Silveston, P. L. *Applied Catalysis a-General* **187**(1), 147–160 (1999).

[14] Zanthoff, H.-W., Jalibert, J.-C., Schuurmann, Y., Slama, P., Herrmann, J.-M., and Mirodatos, C. In *Studies in surface science and catalysis,* Fierro, J., editor. (2000).

[15] Contractor, R. M. *Chemical Engineering Science* **54**(22), 5627–5632 (1999).

[16] Contractor, R. M., Bergna, H. E., Horowitz, H. S., Blackstone, C. M., Malone, B., Torardi, C. C., Griffiths, B., Chowdhry, U., and Sleight, A. W. *Catalysis Today* **1**(1-2), 49–58 (1987).

[17] Contractor, R. M., Anderson, M., Campos, D., Hecquet, G., Kotwica, R., Pham, C., and Simon, M. (1999).

[18] Bohling, R., Drochner, A., Fehlings, M., Konig, D., and Vogel, H. *Chemical Engineering & Technology* **22**(9), 747–750 (1999).

[19] Callejas, C., Soler, J., Herguido, J., Menndez, M., Santamara, J., Avelino Corma, F. V. M. S. M., and Fierro, J. L. G. In *Studies in Surface Science and Catalysis*, volume Volume 130, 2717–2722. Elsevier (2000). 0167-2991 doi: DOI: 10.1016/S0167-2991(00)80881-2.

[20] Burch, R. and Swarnakar, R. *Applied Catalysis* **70**(1), 129–148 (1991).

[21] Zeng, Y., Tamhankar, S., Ramprasad, N., Fitch, F., Acharya, D., and Wolf, R. *Chemical Engineering Science* **58**(3-6), 577–582 (2003).

[22] Trovarelli, A. *Catalysis by Ceria and Related Materials.* Imperial College Press, (2002).

[23] Duwez, P. and Odell, F. *Journal of the American Ceramic Society* **33**(9), 274–283 (1950).

[24] Duran, P., Gonzalez, M., Moure, C., Jurado, J. R., and Pascual, C. *Journal of Materials Science* **25**(12), 5001–5006 (1990).

[25] Meriani, S. *Materials Science and Engineering a-Structural Materials Properties Microstructure and Processing* **109**, 121–130 (1989).

[26] Meriani, S. *Materials Science and Engineering* **71**(1-2), 369–370 (1985).

[27] Tani, E., Yoshimura, M., and Somiya, S. *Journal of the American Ceramic Society* **66**(7), 506–510 (1983).

[28] Yashima, M., Takashina, H., Kakihana, M., and Yoshimura, M. *Journal of the American Ceramic Society* **77**(7), 1869–1874 (1994).

[29] Yashima, M., Morimoto, K., Ishizawa, N., and Yoshimura, M. *Journal of the American Ceramic Society* **76**(7), 1745–1750 (1993).

[30] Yashima, M., Morimoto, K., Ishizawa, N., and Yoshimura, M. *Journal of the American Ceramic Society* **76**(11), 2865–2868 (1993).

[31] Yashima, M., Ohtake, K., Arashi, H., Kakihana, M., and Yoshimura, M. *Journal of Applied Physics* **74**(12), 7603–7605 (1993).

[32] Shannon, R. D. *Acta Crystallographica Section A* **32**(SEP1), 751–767 (1976).

[33] Lamas, D. G., Fuentes, R. O., Fabregas, I. O., de Rapp, M. E. F., Lascalea, G. E., Casanova, J. R., de Reca, N. E. W., and Craievich, A. F. *Journal of Applied Crystallography* **38**, 867–873 (2005).

[34] Bunluesin, T., Gorte, R. J., and Graham, G. W. *Applied Catalysis B-Environmental* **15**(1-2), 107–114 (1998).

[35] Craciun, R., Shereck, B., and Gorte, R. J. *Catalysis Letters* **51**(3-4), 149–153 (1998).

[36] Heck, R. M. and Farrauto, R. J. *Applied Catalysis a-General* **221**(1-2), 443–457 (2001).

[37] Kaspar, J., Fornasiero, P., and Graziani, M. *Catalysis Today* **50**(2), 285–298 (1999).

REFERENCES

[38] Ozawa, M., Kimura, M., and Isogai, A. *Journal of Alloys and Compounds* **193**(1-2), 73–75 (1993).

[39] Shelef, M., Graham, W. G., and McCabe, W. R. In *Catalysis by Ceria and Related Materials,* Trovarelli, A., editor, 343–375. Imperial College Press, London (2002).

[40] Liu, W. and Flytzani-Stephanopoulos, M. *Chemical Engineering Journal* **64**(2), 283–294 (1996).

[41] Scire, S., Minico, S., Crisafulli, C., Satriano, C., and Pistone, A. *Applied Catalysis B-Environmental* **40**(1), 43–49 (2003).

[42] Sedmak, G., Hocevar, S., and Levec, J. *Journal of Catalysis* **213**(2), 135–150 (2003).

[43] Trovarelli, A., de Leitenburg, C., Boaro, M., and Dolcetti, G. *Catalysis Today* **50**(2), 353–367 (1999).

[44] Kim, T., Vohs, J. M., and Gorte, R. J. *Industrial & Engineering Chemistry Research* **45**(16), 5561–5565 (2005).

[45] Goldschmidt, V. M. *Naturwissenschaften* **14**, 477–485 (1926).

[46] Kiennemann, A., Petit, C., Roger, A. C., and Pitchon, V. *Current Topics in Catalysis* **3**, 147–160 (2002).

[47] Mizusaki, J., Mima, Y., Yamauchi, S., Fueki, K., and Tagawa, H. *Journal of Solid State Chemistry* **80**(1), 102–111 (1989).

[48] Mizusaki, J., Yoshihiro, M., Yamauchi, S., and Fueki, K. *Journal of Solid State Chemistry* **58**(2), 257–266 (1985).

[49] Stolen, S., Bakken, E., and Mohn, C. E. *Physical Chemistry Chemical Physics* **8**(4), 429–447 (2006).

[50] Negas, T. and Roth, R. S. *Journal of Solid State Chemistry* **3**(3), 323–& (1971).

[51] Bakken, E., Norby, T., and Stolen, S. *Journal of Materials Chemistry* **12**(2), 317–323 (2002).

[52] Kuroda, K., Shinozaki, K., Uematsu, K., Mizutani, N., and Kato, M. *Journal of the American Ceramic Society* **63**(1-2), 109–110 (1980).

[53] Mizusaki, J., Tagawa, H., Naraya, K., and Sasamoto, T. *Solid State Ionics* **49**, 111–118 (1991).

[54] Dai, X., Yu, C., Li, R., Wu, Q., and Hao, Z. *Journal of Rare Earths* **26**(1), 76–80 (2008).

[55] Dai, X., Yu, C., Li, R., Wu, Q., Shi, K., and Hao, Z. *Journal of Rare Earths* **26**(3), 341–346 (2008).

[56] Dai, X., Yu, C., and Wu, Q. *Journal of Natural Gas Chemistry* **17**(4), 415–418 (2008).

[57] Dai, X. P., Li, R. J., Yu, C. C., and Hao, Z. P. *The Journal of Physical Chemistry B* **110**(45), 22525–22531 (2006).

[58] Dai, X. P., Wu, Q., Li, R. J., Yu, C. C., and Hao, Z. P. **110**(51), 25856–25862 (2006).

[59] Kharton, V. V., Patrakeev, M. V., Waerenborgh, J. C., Sobyanin, V. A., Veniaminov, S. A., Yaremchenko, A. A., Gaczynski, P., Belyaev, V. D., Semin, G. L., and Frade, J. R. *Solid State Sciences* **7**(11), 1344–1352 (2005).

[60] Li, K. Z., Wang, H., Wei, Y. G., and Yan, D. X. *Chemical Engineering Journal* **156**(3), 512–518.

[61] Li, R., Yu, C., and Shen, S. *J. Nat. Gas Chem.* **11**(3-4), 137–144 (2002).

[62] Li, R., Yu, C., Zhu, G., and Shen, S. *Petroleum Science* **2**(1), 19–23 (2005).

[63] Mihai, O., Chen, D., and Holmen, A. *Industrial & Engineering Chemistry Research* .

[64] Rietveld, H. M. *Journal of Applied Crystallography* **2**, 65–& (1969).

[65] Rietveld, H. M. *Acta Crystallographica* **22**, 151–& (1967).

[66] Toby, B. H. *Journal of Applied Crystallography* **34**, 210–213 (2001).

REFERENCES

[67] Patterson, A. L. *Phys. Rev.* **56**(10), 978–982 Nov (1939).

[68] Otsuka, K., Wang, Y., Sunada, E., and Yamanaka, I. *Journal of Catalysis* **175**(2), 152–160 (1998).

[69] Fathi, M., Bjorgum, E., Viig, T., and Rokstad, O. A. *Catalysis Today* **63**(2-4), 489–497 (2000).

[70] Karen, P. *Journal of Solid State Chemistry* **179**(10), 3167–3183 (2006).

[71] Jalibert, J. C., Fathi, M., Rokstad, O. A., and Holmen, A. *Stud. Surf. Sci. Catal.* **136**(Natural Gas Conversion VI), 301–306 (2001).

[72] Otsuka, K., Ushiyama, T., and Yamanaka, I. *Chemistry Letters* (9), 1517–20 (1993).

[73] Otsuka, K., Wang, Y., and Nakamura, M. *Applied Catalysis, A: General* **183**(2), 317–324 (1999).

[74] Pantu, P., Kim, K., and Gavalas, G. R. *Applied Catalysis, A: General* **193**(1,2), 203–214 (2000).

[75] Readman, J. E., Olafsen, A., Larring, Y., and Blom, R. *Journal of Materials Chemistry* **15**(19), 1931–1937 (2005).

[76] Shah, P. R., Kim, T., Zhou, G., Fornasiero, P., and Gorte, R. J. *Chemistry of Materials* **18**(22), 5363–5369 (2006).

[77] Zhou, G., Shah, P. R., Kim, T., Fornasiero, P., and Gorte, R. J. *Catalysis Today* **123**(1-4), 86–93 (2007).

[78] Mizusaki, J., Yoshihiro, M., Yamauchi, S., and Fueki, K. *Journal of Solid State Chemistry* **58**(2), 257 – 266 (1985).

[79] *Thermodynamic Research Center Physical and Chemical division NIST, National Institute of Standards and Technology* .

I

II

Catal Lett (2011) 141:8–14
DOI 10.1007/s10562-010-0441-x

Thermodynamic Control of Product Formation During the Reaction Between CH_4 and Pt Promoted Ceria-zirconia Solid Solutions

Federica Mudu · Bjørnar Arstad · Helmer Fjellvåg · Unni Olsbye

Received: 30 June 2010 / Accepted: 20 August 2010 / Published online: 17 September 2010

Abstract The reaction between CH_4 and framework oxygen of Pt promoted $Ce_xZr_{1-x}O_2$ ($x = 0.25, 0.5, 0.75, 1$) solid solutions was studied at 873 K for syngas ($CO + H_2$) production. The homogeneity and cubic/tetragonal structure of the solid solutions were confirmed by powder X-ray diffraction. The thermodynamic properties of the solid solutions, connected with Ce^{4+}/Ce^{3+} redox reactions, were measured by titrating the oxygen content of the oxides after equilibration in flowing mixtures of H_2 and CO_2 with $10^{-31} < pO_2 < 10^{-22}$ atm. The transient reactions between the oxides and discrete pulses of CH_4, as well as of isotopically labeled $^{13}CH_4 + {}^{12}CO$ mixtures (limited to the material with $x = 0.25$) were investigated and reactivity, conversion and selectivity were measured. A strong correlation between the thermodynamic properties of the oxides and the syngas selectivity was found. The ^{13}C scrambling in CO and CO_2 during co-feed experiments confirmed equilibration of these molecules with the oxides surfaces.

Keywords Cerium oxide · Methane partial oxidation · Degree of reduction

1 Introduction

Ceria based oxides have a great potential for catalytic applications, and have during the last years been investigated for processes like water gas shift, supports for reforming catalysts, VOCs catalytic combustion, CO preferential oxidation and conversion of emission gases [1–10]. The behavior of ceria based oxides in catalysis is typically connected with the redox couple Ce^{4+}/Ce^{3+} and the consequent reversible oxygen storage capacity. One reaction where the reducibility of cerium oxide plays a central role is the conversion of CH_4 to syngas (CO and H_2) by framework oxygen (Eq. 1 below), and subsequent regeneration of the CeO_2 with air (Eq. 2). This approach to methane conversion might become particularly relevant in gas to liquids (GTL) offshore units, where the direct high-temperature reaction of CH_4 with O_2 (or air) has technological and risk challenges.

$$yCH_4 + MO_x = yCO + 2yH_2 + MO_{x-y} \quad (1)$$

$$MO_{x-y} + \frac{1}{2}yO_2 = MO_x \quad (2)$$

The use of cerium oxide in this partial oxidation reaction was first reported by Otsuka et al. [11]. Later, the same authors published a report where Pt/CeO_2 reactivity was investigated with the aim of obtaining insights in the reaction mechanism [12]. The following set of reactions were proposed:

Electronic supplementary material The online version of this article (doi:10.1007/s10562-010-0441-x) contains supplementary material, which is available to authorized users.

F. Mudu · H. Fjellvåg · U. Olsbye (✉)
Centre of Material Science and Nanotechnology, Department of Chemistry, University of Oslo, P.O. Box 1126, Blindern, Oslo 0318, Norway
e-mail: unni.olsbye@kjemi.uio.no

B. Arstad
SINTEF Materials and Chemistry, Forskningsveien 1, 0314 Blindern, Oslo, Norway

B. Arstad · H. Fjellvåg · U. Olsbye
Department of Chemistry, inGAP Centre of Research-Based Innovation, University of Oslo, P.O. Box 1126, Blindern, Oslo 0318, Norway

$$CH_4 \rightarrow C(a) + 4H(a) \quad (3)$$

$$4H(a) \rightarrow 2H_2 \quad (4)$$

$$xC(a) + CeO_2 \rightarrow xCO + CeO_{2-x} \quad (5)$$

The recombination and desorption of hydrogen atoms was suggested as possible rate-determining steps but no details were given on the CO_2/CO selectivity. Subsequently, the use of CeO_2–ZrO_2 solid solutions was introduced for the same reaction by the same authors. In this case, CH_4 decomposition was suggested as the rate-determining step in the early stage of the reaction, and Zr^{4+} was pointed out as the catalytic center for methane activation [13]. At a later reaction stage, coke formation was observed and this was ascribed to the decrease in concentration or activity of the surface oxygen.

The relationship between selectivity towards syngas and degree of oxide reduction was first reported by Pantu et al. for Pt/CeO_2–ZrO_2 as catalyst and oxygen source. The selectivity was reported to vary with the composition of the CeO_2–ZrO_2 solid solution [14]. Generally, introduction of zirconia in the $Ce_xZr_{1-x}O_2$ solid solution reduced the selectivity toward syngas (i.e., more CO_2 and H_2O being formed). No difference in activity was reported as a function of Pt loading. In that work, methane activation and solid state oxygen diffusion were presented as two possible rate determining steps. However, none of these hypotheses could fit with the experimental results. Nevertheless, the authors speculated that the CO selectivity might be controlled by the relative rate of the CO oxidation and desorption reactions, and that the rate of CO oxidation is sensitive to the degree of oxide reduction. Fathi et al. investigated CeO_2 supported on γ-Al_2O_3 promoted with Pt or Rh for partial oxidation of methane [15, 16]. A relationship between selectivity to syngas and degree of reduction of the oxide was observed.

In spite of the rich literature on ceria based materials and their applications, the key factors governing syngas selectivity, and CH_4 conversion, and their relationship to the redox properties of the reducible oxide are still not clear. It was recently recognized that CeO_2–ZrO_2 solid solutions, compared to pure CeO_2, have dramatically different thermodynamic properties, in addition to the well known effect on their kinetic properties [17–19]. The oxidation enthalpy reported for CeO_2–ZrO_2 solid solutions was approximately 240 kJ/mol lower than for pure CeO_2 [19]. However, no difference in the enthalpy of reduction was observed upon increasing Zr content in the solid solutions and the clear enhancement in reducibility was in this case explained by entropy effects [18, 19].

The aim of the present contribution is to identify and elucidate parameters controlling CH_4 conversion and CO selectivity during cyclic catalytic partial oxidation of methane to syngas over Pt/$Ce_xZr_{1-x}O_2$ catalysts. Four compositions of Pt/$Ce_xZr_{1-x}O_2$ solid solutions were selected and studied during transient reactions with CH_4 pulses or $^{13}CH_4$ + ^{12}CO pulses. Furthermore, the thermodynamic redox properties were measured for the same materials under flowing gas mixtures. The data obtained clearly indicate that the redox properties of the oxides are directly controlling the syngas selectivity. Our results provide new knowledge and highly valuable input for future design of improved materials for the current and similar cyclic oxidative catalytic processes.

2 Experimental

2.1 Material Synthesis

The materials were prepared by dissolving measured amounts of $Ce(NH_4)_2{\cdot}(NO_3)_6$ (Fluka p.a., $\geq$ 99%) and $ZrOCl_2{\cdot}8H_2O$ (Merck p.a., $\geq$ 99%) in water and then mixing the solutions. Subsequently a solution of NH_4OH was added during 15–20 min to precipitate $CeZrO_2$ while stirring at room temperature. The yellowish powders were washed 5–6 times until neutral solution and dried overnight at 373 K. The temperature was then raised to 1073 K and the samples were calcined for 10 h.

The calcined samples were impregnated with Pt by the incipient wetness method. Measured amounts of $(NH_3)Pt(NO_3)_2$ powder (AlfaAesar) were dissolved in water and deposited onto the $CeZrO_2$ materials by incipient wetness impregnation. The samples were then dried overnight at 383 K. The temperature was then raised to 1073 K (5 °C/min) and the samples were calcined at 1073 K for 10 h.

Samples with 100, 75, 50 and 25% CeO_2 impregnated with Pt were named Pt/CeO_2, Pt/75CeZrO_2, Pt/50CeZrO_2, Pt/25CeZrO_2 respectively.

2.2 Material Characterization

Powder X-ray diffraction patterns were recorded with a position sensitive detector using a Siemens Bruker D5000 diffractometer and monochromatic Cu Kα_1 radiation. The average crystallite sizes of the oxidized samples were calculated using the Scherrer equation based on the width of the (101) diffraction peak.

2.3 Equilibrium Measurement

The oxygen non-stoichiometry was measured as a function of pO_2 at 873 K using a method similar to that reported by Kim and coworkers [17]. Data obtained in the present study were compared to those of Kim et al. for similar materials,

confirming that equilibrium was reached for the given material/conditions pairs [17]. The sample (Pt/CeO_2, $Pt/75CeZrO_2$, $Pt/50CeZrO_2$ and $Pt/25CeZrO_2$: 0.30, 0.80, 0.87 and 0.78 g, respectively) was loaded into a tubular quartz reactor (i.d. 8 mm) and heated under air flow (5 mL/min) to 873 K. The gas feed was then switched to a mixture of CO_2 and H_2 (eventually diluted in He to keep a constant flow rate) where a given pO_2 was realized through the equilibrium reactions 4 and 5.

$$CO_2 \leftrightarrow CO + \frac{1}{2}O_2 \cdot pO_2 = \left(K_{eq1}\frac{pCO_2}{pCO}\right)^2 \quad (4)$$

$$H_2O \leftrightarrow H_2 + \frac{1}{2}O_2 \cdot pO_2 = \left(K_{eq2}\frac{pH_2O}{pH_2}\right)^2 \quad (5)$$

In each experiment the sample was subjected to the specific CO_2–H_2–He gas mixture in a continuous flow mode (detailed gas flows and experimental conditions are reported in Table 1), thus at a predetermined pO_2, for 180 min and subsequently flushed with He (90 mL/min) for 30 min. To determine the non-stoichiometry, dry air was thereafter fed (5 mL/min) while using N_2 as internal standard to calculate the amount of adsorbed O_2. The effluent gases were monitored by an online mass spectrometer (Pfeiffer Omnistar), recording the mass numbers (m/z) 4, 14, 18, 28, 32 and 44. The initial oxygen content of the oxides before reacting with CH_4 in the transient tests (after exposure to He, AGA 99.9995%, for 10 min) was measured in a separate experiment. Samples were exposed to a stream of the carrier gas for 10 min and thereafter to air (5 mL/min), N_2 was used as internal standard to calculate the amount of absorbed O_2.

2.4 Transient Catalytic Test (CH_4/O_2)

Catalytic testing was performed in a tubular quartz reactor (i.d. 8 mm) at 873 K and 1 atm pressure. The catalyst (0.1 g, 0.2–0.5 mm diameter) was diluted by quartz (0.4 g, 0.2–0.5 mm). An automated setup equipped with 4-way and 6-way VICI VALCO valves was used. Feed gases (AGA, 99.996%) were used without further purification. The 4-way valve was used to switch between 10% CH_4/He and 10% O_2/He mixtures. The 6-way valve was equipped with a loop (0.25 mL) and used to send discrete pulses of gas under a continuous stream of Ar (30 mL/min), to the reactor. O_2 pulses were sent to the reactor every second minute while the catalyst was heated to 873 K. The sample was equilibrated in He flow for 30 min at 873 K and thereafter subjected to a series of 50 CH_4 pulses (10% CH_4/He, 1.04 μmol CH_4/pulse) followed by a series of 100 O_2 pulses (10% O_2/He, 1.04 μmol O_2/pulse). Effluent gases were monitored by an online mass spectrometer (Pfeiffer Omnistar). Calibration values for quantification of CH_4, CO_2, CO and H_2 were found by sending known pulses of these gases to an empty reactor preheated to 873 K and integrating the area under the peaks of m/z 15, 44, 28 and 2, respectively. The contribution of CO_2 to m/z 28 was accounted for before quantification of CO. Carbon balance was calculated for each pulse as the sum of CO_2, CO and unconverted CH_4. H_2O was quantified as the difference between converted CH_4 and produced H_2(×0.5). The oxygen nonstoichiometry after each CH_4 pulse was calculated from the amount of oxygen released in terms of CO_2, H_2O and CO (Table 2).

Table 1 Experimental details for the equilibrium measurements

CO_2 (mL/min)	H_2 (mL/min)	He (mL/min)	−log p(O_2) (atm)
20	0.5	10	21.5
5	5	20	24.2
1	5	24	25.4
0.1	10	20	28.3
0.03	10	20	28.9
0.01	10	20	30.5

Table 2 Structural details

Sample	Unit cell volume (Å)	Space group	Particle size (Å) (XRD)
CeO_2	158.4	Fm3 m	586
$75CeZrO_2$	76.6	P42/nmcs	87
$50CeZrO_2$	73.7	P42/nmcs	78
$25CeZrO_2$	70.2	P42/nmcs	80

2.5 Transient Catalytic Test ($^{13}CH_4$–CO/Air)

Transient tests between $Pt/Ce_{0.75}Zr_{0.25}O_2$ and $^{13}CH_4$ + ^{12}CO were performed in the same setup as described in Sect. 2.4. Experiments were performed using two different carrier gas flows, 15 and 30 mL/min. The sample was heated to 873 K while air pulses (dry air, 1.04 μmol air/pulse) were sent to the reactor every 2 min. The sample was equilibrated in He flow for 30 min at 873 K and thereafter subjected to a series of 60 $^{13}CH_4$ + ^{12}CO pulses (1.4 μmol $^{13}CH_4$, 1.1 μmol ^{12}CO, in each pulse) followed by a series of 50 air pulses (1.04 μmol air/pulse). The m/z = 2, 4, 12, 13, 14, 15, 16, 17, 18, 28, 29, 44, 45 were monitored by the online mass spectrometer.

In all catalytic tests, irrespective of possible co-feeding of CO, CO selectivity was calculated as: 100% × [p(CO)/(p(CO) + p(CO_2)], while CH_4 conversion was calculated as: 100% × [(p(CH_4)in-p(CH_4)out)/p(CH_4)in]. H_2 selectivity was calculated as 100% × p(H_2)/[2 × (p(CH_4)in-p(CH_4)out)].

Carbon balance was calculated for each pulse as the sum of unconverted CH_4, CO_2 and CO. H_2O was quantified as the difference of the converted CH_4 and the produced H_2.

The statistical $^{13}C/^{12}C$ distribution among the products in $^{13}CH_4/^{12}CO$ co-feed tests was calculated as: $[(p(^{13}CH_4)in \times CH_4 \quad conversion \times 0.01)/((p(^{12}CO)in-p(^{12}CH_4)out)/p(^{12}CO)in)]$. At full CH_4 conversion, the ratio was 1.27.

3 Results

3.1 Material Characterization

3.1.1 Structure

CeO_2 and ZrO_2 form solid solutions for a wide range of compositions and the phase diagram has been extensively studied since the 1950s [20–25]. A monoclinic ($P2_1/c$), a cubic ($Fm3m$) and three tetragonal phases termed t, t' and t'' (all space group $P4_2/nmc$) are reported for temperatures below 1273 K [26–28].Their existence regions are indicated in the upper abscissa in Fig. 1. The three tetragonal phases are characterized by the degree of tetragonal distortion (c/a) and by their nature (t is stable, while t' and t'' are metastable). The distinction between these phases, especially between the t and t', and between t'' and cubic is quite subtle and can hardly be settled by laboratory scale powder X-ray diffraction. By using synchrotron radiation powder XRD, Lamas et al. studied the crystal structure of the CeO_2–ZrO_2 solid solutions and distinguished between tetragonal and cubic phase [29]. In Fig. 1 the pseudo-cubic lattice parameter, defined for the tetragonal phases as

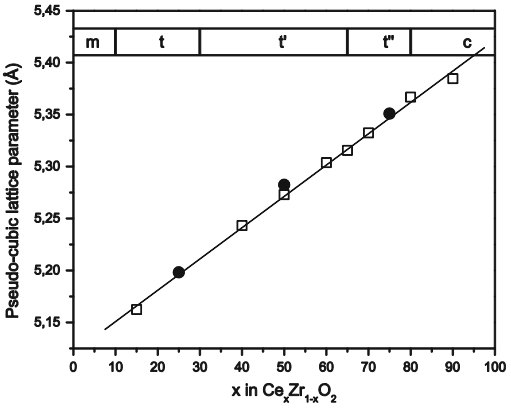

Fig. 1 Measured pseudo cubic lattice parameter for $Ce_xZr_{1-x}O_2$ (*circle*) and as reported in Ref [29] (*square*). Existence regions for the different $CeZrO_2$ crystalline phases are reported in the upper part of the figure [26–28]

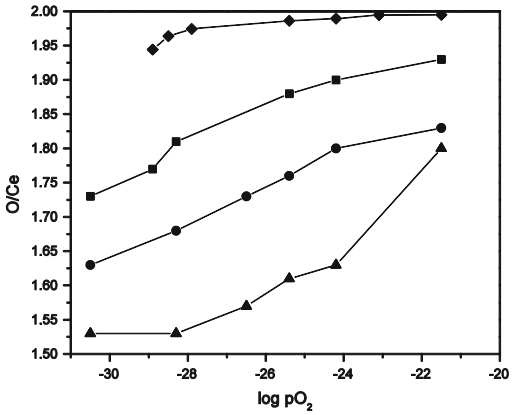

Fig. 2 O/Ce ratio as a function of pO_2 for Pt/CeO_2 (*diamond*), Pt/75$CeZrO_2$ (*square*), Pt/50$CeZrO_2$ (*circle*) and Pt/25$CeZrO_2$ (*triangle*) at 873 K

$^{\circ}a_{average} = \left(2\left(\sqrt{2}a\right) + c\right)/3$, is plotted for the solid solutions $Ce_{0.75}Zr_{0.25}O_2$, $Ce_{0.5}Zr_{0.5}O_2$ and $Ce_{0.25}Zr_{0.75}O_2$ obtained in this work, together with values reported by Lamas et al. [29]. The unit cell volume variation obeys the Vegard's law which indicates incorporation of ZrO_2 into the CeO_2 phase without major additional interactions. A more thorough structural investigation is beyond the scope of this work.

3.1.2 pO_2 Dependency of Oxygen Non-Stoichiometry

Figure 2 shows the oxygen to cerium ratio as a function of pO_2. Since the Zr atoms do not take part in the reduction process, the degree of reduction of the oxide is reported as O/Ce in Fig. 2. When increasing the Zr content of the solid solutions the Ce^{3+}/Ce^{4+} ratio increases at a given pO_2 value. This finding is in agreement with literature data on similar $Ce_xZr_{1-x}O_2$ solid solutions [17–19]. The enhanced reducibility of Ce^{4+} atoms when present in the solid solutions has been explained in terms of a combination of enthalpy and entropy effects [18, 19].

3.2 Reactivity

3.2.1 CH_4/O_2 Pulses

Results from studies of the reaction between the Pt/$Ce_xZr_{1-x}O_2$ oxides and CH_4 pulses are reported as a function of the O/Ce-ratio of the oxide catalyst in Fig. 3. For the fully oxidized samples (O/Ce close to 2), the conversion is close to 100%. However, after repeated CH_4 pulses reacted with the oxide, the CH_4 conversion started to decrease. The specific O/Ce-ratio at which the CH_4

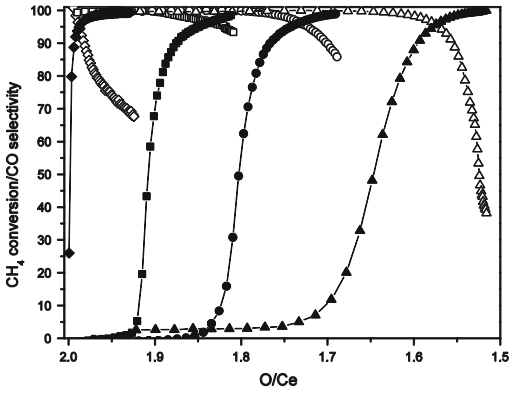

Fig. 3 CH_4 conversion (empty markers) and CO selectivity (full markers) for Pt/CeO_2 (*diamond*), $Pt/75CeZrO_2$ (*square*), $Pt/50CeZrO_2$ (*circle*) and $Pt/25CeZrO_2$ (*triangle*) as a function of O/Ce as measured by CH_4 pulses (873 K, 1.04 μmol/pulse)

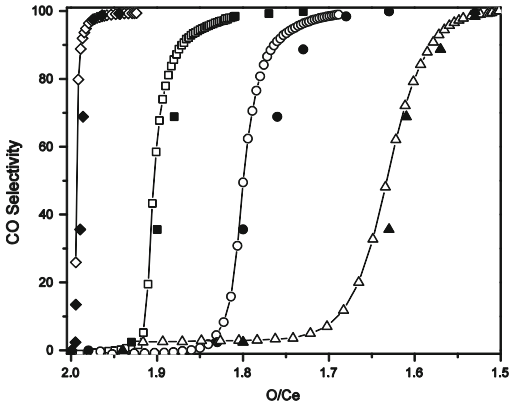

Fig. 4 CO selectivity as a function of O/Ce as measured by flowing titration (full markers, 873 K) and CH_4 pulses (empty markers, 873 K, 1.04 μmol CH_4/pulse) for Pt/CeO_2 (*diamond*), $Pt/75CeZrO_2$ (*square*), $Pt/50CeZrO_2$ (*circle*) and $Pt/25CeZrO_2$ (*triangle*) as a function of O/Ce

conversion starts to decay was found to increase with increasing Zr content. Similarly, the CO (H_2) selectivity varies with the O/Ce ratio, starting at values close to 0% and rapidly increasing to close to 100% after passing a critical O/Ce ratio (Fig. 3). The critical value of O/Ce at which the CO selectivity started to rise, increased with increasing Zr content, just as found with respect to the CH_4 conversion. A peculiar feature of Fig. 3 is that the relationship between CH_4 conversion and CO selectivity is quite similar for all Zr containing samples. A CO selectivity versus CH_4 conversion plot for all samples is included in the additional informations, Fig. 1S.

As reported in Fig. 2 the oxygen potential over the $Ce_xZr_{1-x}O_2$ oxides vary with composition and degree of reduction. In order to compare how this change correlates with the observed variation in CO selectivity, the pO_2 versus O/Ce ratio data in Fig. 2 have been converted to values for equilibrium CO selectivity versus O/Ce ratio according to reaction (6). The transformed data are plotted together with the observed CO selectivity in Fig. 4.

$$CO_2 \leftrightarrow CO + \frac{1}{2}O_2 \qquad \frac{pCO}{pCO + pCO_2} = 1 + \frac{H_{eq}}{pO_2^{1/2}} \qquad (6)$$

Indeed, a good agreement was observed between the theoretically calculated CO selectivity (Eq. 3) and the CO selectivity measured during the reaction of CH_4 with the oxide. This suggests that CO selectivity is determined by the thermodynamic redox properties of the oxide.

Through investigation of the data in Fig. 4 showed that the experimental data were slightly shifted to the left of the predicted data, implying slightly higher CO selectivities than predicted from thermodynamics, especially for the $Pt/50CeZrO_2$ material. If our hypothesis of a thermodynamically determined CO selectivity holds, this result indicates that oxygen diffusion from the bulk to the surface is too slow to maintain the same oxygen stoichiometry throughout the $nCeZrO_{2-x}$ materials under the applied test conditions, i.e., that the surface was depleted in oxygen compared to the amount of bulk oxygen.

Accumulated data for C deposition, O consumption, CO, H_2 and CO_2 production, as well as average CH_4 conversions and CO selectivities over a sequence of 50 CH_4 pulses for each material are summarized in Table 3. The amount of CO_2 produced during the pulse series increased significantly when introducing Zr into ceria. As a consequence, the average CO yield over the pulse series decreased with increasing Zr content. Only the sample with highest Zr content gave detectable amounts of C deposition during a sequence of 50 pulses.

Overall, undoped ceria appears to possess the best potential as a support material for the cyclic catalytic partial oxidation reaction under the conditions studied here.

3.2.2 ($^{13}CH_4$+^{12}CO)/Air Pulses

Conversion, selectivity and isotope distribution for the reaction between pulses containing a mixture of $^{13}CH_4$ and ^{12}CO over $Pt/25CeZrO_2$ are reported in Fig. 5. Experiments were performed with two different residence times in order to confirm or exclude kinetic effects. He flows of 15 and 30 mL/min (as in the standard pulse experiments reported in Sect. 3.2.1) were used; the results are reported in Fig. 5a and b, respectively. An expanded view of the second part of the same tests is shown in Fig. 4S. For some pulses the amount of one or more of the species was too small for accurate quantification of the ^{13}C distribution

Table 3 Pulse test results. Accumulated carbon deposition and oxygen consumption during 50 methane pulses

Sample	CH_4 Conversion (%)	CO Selectivity (%)	C Deposited ($\mu mol/g^{-1}$)	O Used ($\mu mol/g^{-1}$)	CO_2 ($\mu mol/g^{-1}$)	CO ($\mu mol/g^{-1}$)	H_2 ($\mu mol/g^{-1}$)
$BulkCeO_2$	78	96	<1	44	2	37	76
$75CeZrO_2$	98	69	<1	90	14	33	68
$50CeZrO_2$	97	63	<1	99	17	30	62
$25CeZrO_2$	80	69	3	83	16	19	45

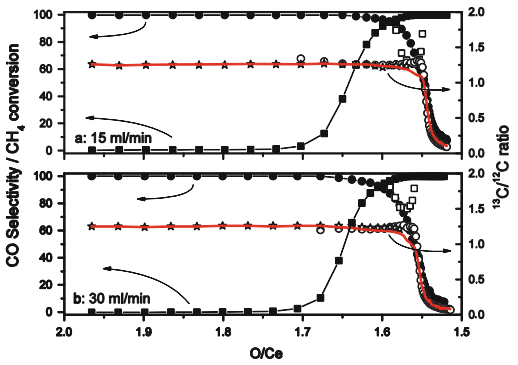

Fig. 5 CH_4 conversion (*circle*), CO selectivity (*square*) and statistical $^{13}C/^{12}C$ ratio (*solid line*), together with $^{13}CH_4/^{12}CH_4$ (*square*), $^{13}CO/^{12}CO$ (*circle*) and $^{13}CO_2/^{12}CO_2$ (*star*) as a function of O/Ce over $Pt/25CeZrO_2$

(i.e., pulses where CH_4 conversion was close to 100% or CO selectivity close to 0%). Hence, the ^{13}C distribution is reported discontinuously. Statistical $^{13}C/^{12}C$ ratio (see experimental section) is reported, as a continuous red line in the same figures.

A comparison between the conversion and selectivity curves at the longer and shorter residence times (Fig. 5a and b, respectively) shows that the two curves cross each other at very similar O/Ce ratios at both residence times. It is interesting to note that at both residence times the $^{13}C/^{12}C$ ratio in CO and CO_2 corresponds to the statistical $^{13}C/^{12}C$ ratio in the whole range studied with only a small deviation during a O/Ce ratio of $\sim$1.57–1.55. This implies that equilibration between the two products takes place in the whole O/Ce range. This observation supports the conclusion drawn above, i.e.; that the syngas selectivity in the title reaction is determined by thermodynamics and not by kinetics. On the other hand, the $^{13}C/^{12}C$ ratio in CH_4 changed significantly during the pulse sequence. For both residence times, at high O/Ce, the $^{13}CH_4$ conversion was nearly complete, and the $^{13}C/^{12}C$ ratio in CH_4 could not be determined. When $^{13}CH_4$ conversion started to drop, at the longer residence time (Fig. 5a) $^{13}C/^{12}C$ ratio in CH_4 went through a minimum of 1.25 at an O/Ce ratio of 1.57. At the shorter residence time (Fig. 5b and 4S) the $^{13}C/^{12}C$ ratio went through a similar change, however with a minimum at a higher $^{13}C/^{12}C$ value; approximately 1.5. The decrease in $^{13}C/^{12}C$ ratio in methane with oxygen depletion might suggest a change in the rate-determining step of reaction, from reaction (3) at high O contents to a later reaction step at lower O contents. The subsequent increase in ^{13}C content in methane at even lower O contents, observed at both residence times, would suggest that even the back formation of methane was deactivated at lower O contents.

It has previously been suggested that the relative rates between CO desorption and further oxidation might control the CO selectivity in the title reaction over ceria-based catalysts [14]. Our observation of complete equilibration of C-containing products contradicts this view. We clearly propose to shift focus from kinetic to thermodynamic effects when searching for optimum cyclic partial oxidation catalysts. The present work thus represents an important step forward towards a better understanding of the connection between thermodynamic bulk properties of reducible oxides and their catalytic activity. The results now available suggest that design of improved oxidants for the conversion of CH_4 to syngas should undergo reduction in a suitable pO_2 range, i.e., below 10^{-25} atm at 873 K.

4 Conclusions

The relationship between methane oxidation to products and the degree of oxide reduction was studied for a series of Pt promoted $Ce_xZr_{1-x}O_2$ materials by combining conversion-selectivity data and thermodynamic measurements in a lab scale tubular reactor.

The product distribution over the Pt promoted $Ce_xZr_{1-x}O_2$ solid solution was found to strongly correlate with the thermodynamic bulk properties of the reducible oxide. The present findings provide important input for the further development of selective reducible oxides for divided catalytic processes.

Acknowledgments This publication is part of the Remote Gas project (168223/S30), performed under the strategic program Petromaks of The Research Council of Norway. The authors acknowledge the additional partners; Statoil, UOP, Bayerngas Norge, Aker Solutions, DNV for support. Aud Spjelkavik (SINTEF) is acknowledged for synthesis of the materials.

References

1. Bunluesin T, Gorte RJ, Graham GW (1998) Appl Catal B-Environ 15:107
2. Craciun R, Shereck B, Gorte RJ (1998) Catal Lett 51:149
3. Heck RM, Farrauto RJ (2001) Appl Catal A-Gen 221:443
4. Ozawa M, Kimura M, Isogai A (1993) J Alloy Compd 193:73
5. Shelef M, Graham WG, McCabe WR (2002) In: Trovarelli A (ed) Catalysis by Ceria and Related Materials. Imperial College Press, London, p 343
6. Kaspar J, Fornasiero P, Graziani M (1999) Catal Today 50:285
7. Trovarelli A, de Leitenburg C, Boaro M, Dolcetti G (1999) Catal Today 50:353
8. Scire S, Minico S, Crisafulli C, Satriano C, Pistone A (2003) Appl Catal B-Environ 40:43
9. Sedmak G, Hocevar S, Levec J (2003) J Catal 213:135
10. Liu W, Flytzani-Stephanopoulos M (1996) Chem Eng J 64:283
11. Otsuka K, Ushiyama T and Yamanaka I (1993) Chem Lett 1517
12. Otsuka K, Wang Y, Sunada E, Yamanaka I (1998) J Catal 175: 152
13. Otsuka K, Wang Y, Nakamura M (1999) Appl Catal A-Gen 183: 317
14. Pantu P, Kim K, Gavalas GR (2000) Appl Catal A-Gen 193:203
15. Fathi M, Bjorgum E, Viig T, Rokstad OA (2000) Catal Today 63:489
16. Jalibert JC, Fathi M, Rokstad OA, Holmen A (2001) Stud Surf Sci Catal 136:301
17. Kim T, Vohs JM, Gorte RJ (2005) Ind Eng Chem Res 45:5561
18. Shah PR, Kim T, Zhou G, Fornasiero P, Gorte RJ (2006) Chem Mater 18:5363
19. Zhou G, Shah PR, Kim T, Fornasiero P, Gorte RJ (2007) Catal Today 123:86
20. Duwez P, Odell F (1950) J Am Ceram Soc 33:274
21. Meriani S (1985) J Mater Sci Eng 71:369
22. Yashima M, Takashina H, Kakihana M, Yoshimura M (1994) J Am Ceram Soc 77:1869
23. Meriani S (1989) Mater Sci Eng A-Struct 109:121
24. Duran P, Gonzalez M, Moure C, Jurado JR, Pascual C (1990) J Mater Sci 25:5001
25. Tani E, Yoshimura M, Somiya S (1983) J Am Ceram Soc 66:506
26. Yashima M, Morimoto K, Ishizawa N, Yoshimura M (1993) J Am Ceram Soc 76:1745
27. Yashima M, Morimoto K, Ishizawa N, Yoshimura M (1993) J Am Ceram Soc 76:2865
28. Yashima M, Ohtake K, Arashi H, Kakihana M, Yoshimura M (1993) J Appl Phys 74:7603
29. Lamas DG, Fuentes RO, Fabregas IO, de Rapp MEF, Lascalea GE, Casanova JR, de Reca NEW, Craievich AF (2005) J Appl Crystallogr 38:867

III